3 Part 2: Plant Trials

3.1 Background

From Part 1 parameters affecting the generation of fines (-106µm fraction) appear to be the amount of silicates ($SiO_2+Al_2O_{3(glass)}+CaO$) in the slag, tapping rate, the cooling method (block yield), specific surface area after cooling and the equivalent $\%Ti_2O_3$. Similarly the residual coarse material (+850µm fraction) appears to depend primarily on specific surface area after cooling, and on block yield. The objective of the plant (industrial) trials was therefore to test these observations from the pilot-plant trials with regard to the effects of the tapping rate, cooling method and slag composition. A further objective of the plant trials was to gain further insight into the mechanism(s) driving final slag product particle size distributions.

The flexibility of parameters needs to be understood in context of the plant constraints: the ($SiO_2+Al_2O_{3(glass)}+CaO$) is a function of the orebody and to a limited extent of the upstream beneficiation processes. The specific surface area of the block is a function of the block shape and mass. These two parameters are determined by the slag pot shape and capacity – therefore this is not a controllable variable within the logistics of the existing plant either, at least not without extensive capital re-investment. The slag Ti_2O_3 content is a function of the required $\%TiO_2$ set by market specifications and the ilmenite quality fed (and the ilmenite quality in turn is a function of upstream beneficiation and the orebody). Of the above variables tapping rate, and to an extent the cooling method and ilmenite quality, are thus the only controllable (or partially controllable) parameters within the capabilities of the existing plant design.

3.2 Block selection

Four blocks were selected for the plant trials – two blocks from the same tap having individual tapping rates of 3.63 t/min and 3.70 t/min respectively, and two more blocks from another tap, having relatively low tapping rates of 0.96 t/min and 1.29 t/min respectively. (Typical tapping rates on the industrial plant vary from 0.5 t/min to 4 t/min). Selecting the four blocks from two taps enabled a narrower spread in the compositional differences between the four blocks. The compositions and tapping rates of the four blocks are shown in Table 7. The $\%Ti_2O_3$ was calculated from the correlation shown in Figure 26. The linear equation on the left hand side of Figure 26 is derived from the plant data, while the right hand side equation represents the pilot plant data.

Following tapping, the four blocks were initially left to cool in the pots, with natural air cooling only. After this primary cooling period of 17 to 19 hours, the blocks were tipped out of the pots, transported to the block yard and water cooled with spray water. After 3 days the water sprays of lane 1 (L1 blocks) were closed and the block surface temperatures were recorded using a manual optical pyrometer (see results in Figure 27). In lane 2 (L2 blocks) the water sprays were left on for the full 10 days. Unfortunately, due to windy conditions, water was occasionally sprayed from lane 2 over into lane 1, causing the lane 1 blocks to receive limited cooling water, while the side of the lane 2 blocks (facing the oncoming wind) lost its water cooling.

Table 7 Details of the four blocks selected for the plant trials.

Block number	Tapping rate (ton/min)	%FeO (equivalent %FeO)	Equivalent $\%TiO_2$	$\%Ti_2O_3$ (calculated) (equivalent $\%Ti_2O_3$, calculated)	$\%(SiO_2+Al_2O_{3(glass)}+CaO)$	Cooling method (wc: water cooling; ac: air cooling)
L1R9	3.64	9.90 (13.43)	86.42	30.68 (32.16)	1.638	3 days wc 7 days ac
L2R9	3.70	10.04 (13.58)	86.17	30.45 (31.92)	1.643	10 days wc
L1R11	0.96	10.35 (13.92)	86.43	29.95 (31.44)	1.678	3 days wc 7 days ac
L2R11	1.29	10.45 (14.01)	86.31	29.78 (31.28)	1.671	10 days wc

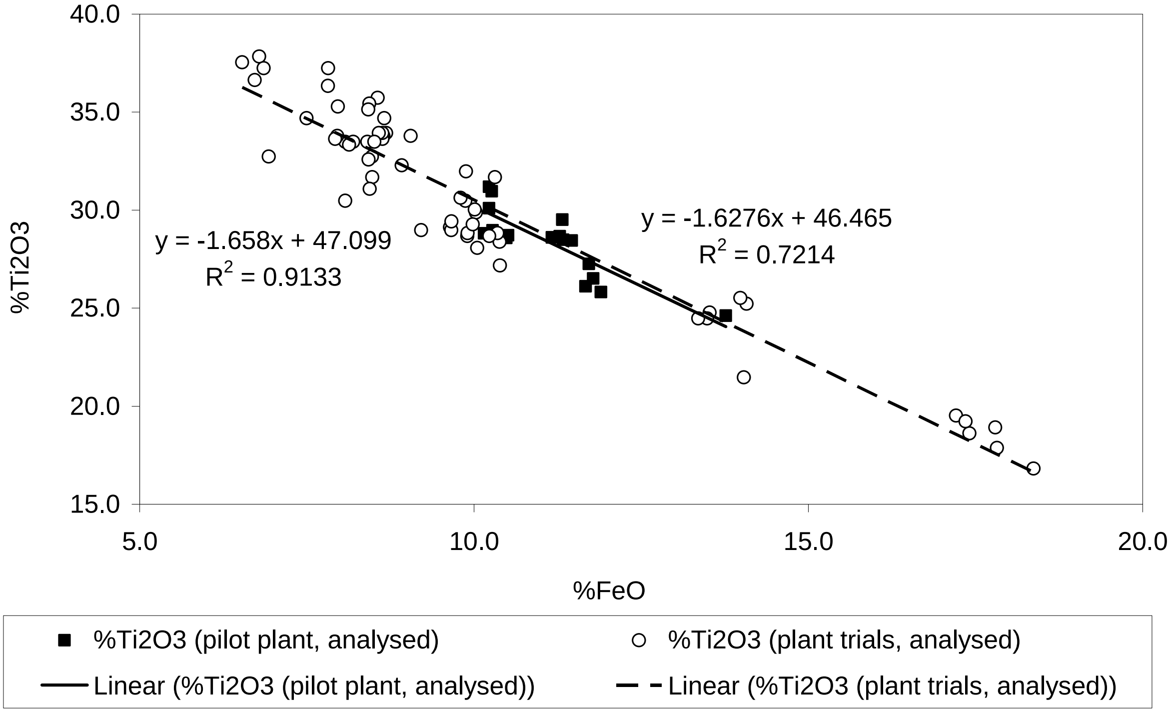

Figure 26 Correlation between %FeO and $\%Ti_2O_3$ for pilot plant slags (solid squares and line; equation on right hand side) and plant slags (open circles and dotted line; equation on left hand side).

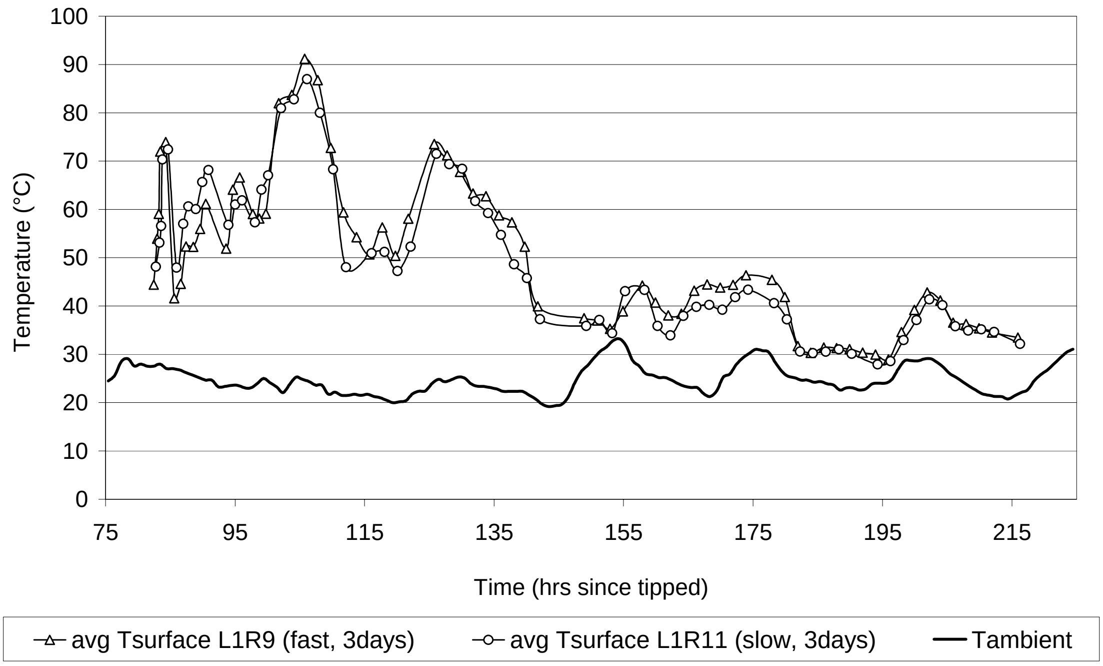

Figure 27 Average surface temperature of blocks L1R9 and L1R11 after closure of the cooling water.

Figure 28 Photograph of an industrial-size block showing fine decrepitated material and large chunks breaking off from the block corners. As an indication of scale, the bottom diameter of the block is approximately 1.8 to 2 m.

During the 10 days of cooling, limited decrepitation occurred with all four blocks. In addition, relatively large chunks – from 10 mm up to 400 mm – broke off from the block corners. Both these two types of block yard remains are visible in Figure 28. After 10 days of cooling, the intact part of all four blocks was broken individually with the hydraulic hammer. The -400 mm fraction passed through the static grizzly to the jaw crusher with a closed side setting of

-45 mm. The jaw crusher product was passed over a 50 mm screen with the oversize fraction being circulated back to the jaw crusher. The undersize (and day bin feed) was sampled with a hammer sampler and sent to the Exxaro Research and Development laboratories for further testwork. Care was taken to run the equipment clean between processing the four blocks. (Refer to Figure 1 for a block diagram of the Slag Plant process flow). The particle size distributions of the block yard remains and jaw crusher product for the four blocks are shown in Figure 29 and Figure 31 respectively.

Since no mass measurement facility exists between the block yard and the first point of entry into the Slag Plant (static grizzly), no mass measurement of the blocks was done at this point.

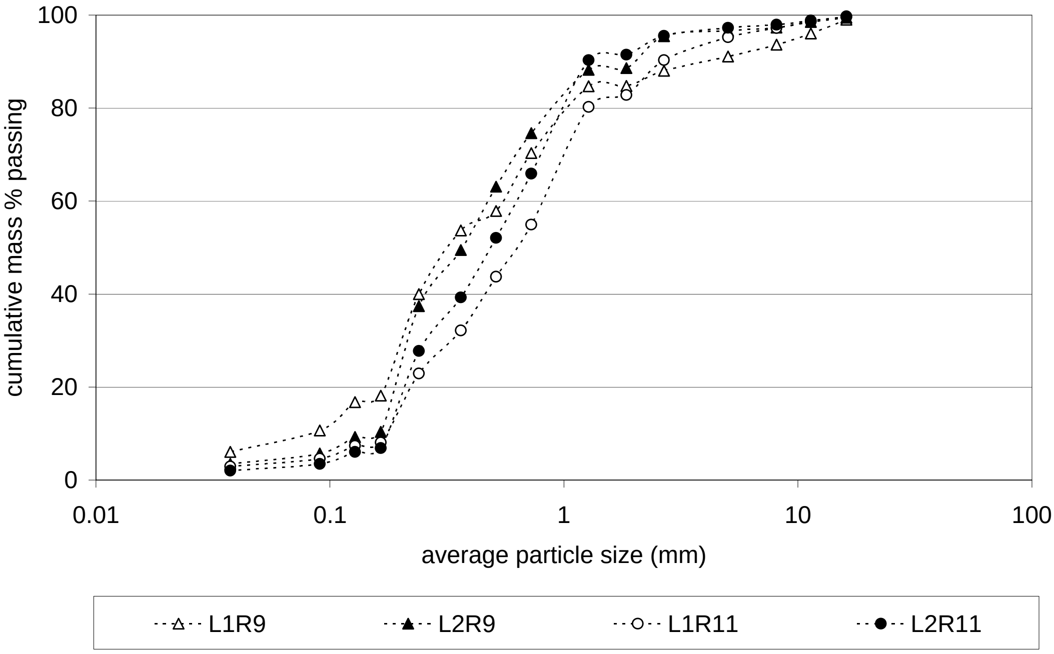

Figure 29 Particle size distribution of the block yard remains – decrepitated material and coarser broken-off sections.

3.3 Tumbling tests

Tumbling tests were used to determine the tendency of the slag to break down due to abrasion between slag particles. This form of breakdown typically occurs during materials handling – mainly at transfer points and mass movement within bins of the plant.

Particle breakdown during materials handling within the plant is not problematic in itself; however, when this breakdown increases the fines fraction (-106 µm) of the slag, it reduces the ratio of higher vs. lower value product produced from the plant. On the other hand, any coarse material (+850 µm) resisting breakdown (either during handling, crushing or milling according to the process (Figure 1), increases the need for higher circulating loads which in turn increases the opportunity for indirect fines generation.

A sample with good tumbling characteristics will therefore show some breakdown, but the size distribution would tend to stabilise after a certain degree of tumbling, with little further breakdown. The fines generated at this point must ideally be as low as possible. Good tumbling characteristics will furthermore be seen where the coarse material breaks down to below 850 µm within the very first material handling steps.

3.3.1 Method

In the first series of tests, five 15 kg sub-samples were riffled from the samples taken as described in section 3.2 and autogenously tumbled for 100, 200, 500, 1000 and 2000 revolutions each. The tumbling mill had an internal diameter of 1,000 mm and an internal length of 500 mm. Two steel angle lifters were positioned 180° apart longitudinally on the inside of the drum. The rotation speed of the drum was 25±1 rpm. The particle size distribution for each sample was determined before and after each test utilising the Canadian Standard Sieve Series[25] between 45 mm and 75 µm. Figure 30 shows the feed and product size distributions for block L1R11 (slow tapping rate, 3 days water cooling); significant variance is apparent in the particle size distributions of the samples taken from each of the four blocks.

The average particle size distribution for each block together with a 90% confidence interval for each size fraction is shown in Figure 31. The particle size distributions of blocks L1R9 (higher tapping rate, 3 days water cooling) and L1R11 (low tapping rate, 3 days water cooling) differ significantly, with those of blocks L2R9 (higher tapping rate, 10 days water cooling) and L2R11 (low tapping rate, 10 days water cooling) being very much the same.

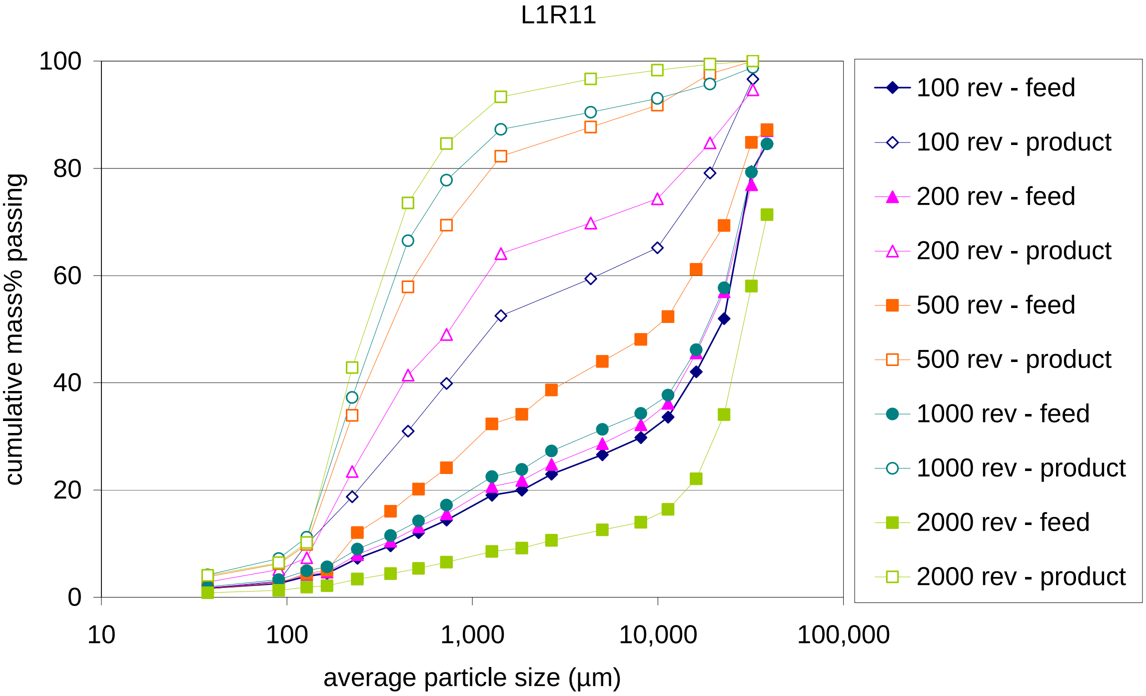

Figure 30 Particle size distribution of the feed to and product material from the tumbling testwork done on block L1R11 (slow, 10 days).

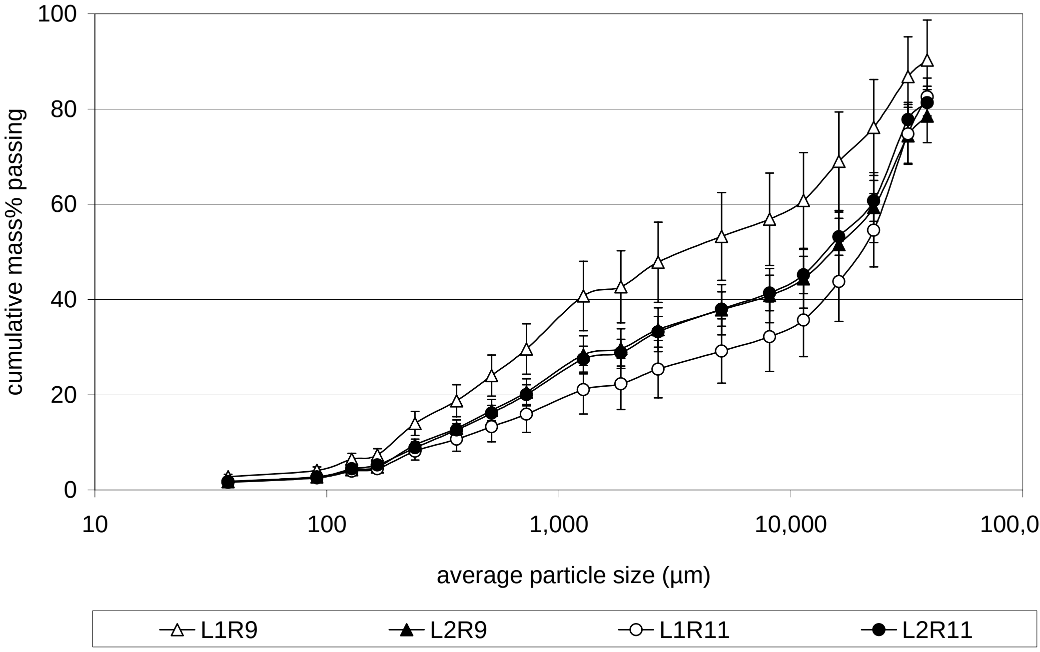

Figure 31 Average particle size distribution of the four blocks (90% confidence intervals shown). Triangles represent higher tapping rates, while circles represent lower tapping rates. Open symbols of 3 days water cooling; solid symbols for 10 days water cooling.

3.3.2 Results

The particle size distributions of the feed and tumble test products, shown as mass percentages retained, are given in Figure 32. A general shift in the peaks of the particle size distribution occurs for all four blocks: after 100 revolutions the +40 mm fraction is reduced considerably, with a substantial increase in the mass percentages for the -850 µm range. After 200 revolutions the peaks at the +850 µm and 300 µm size fractions increased at the expense of the +25 mm peak. From 1000 revolutions onwards, the +25 mm peak continued to decrease. However, the +850 µm peak now started to decrease, yielding an increase in the +600 to +106 µm range. With regard to specifically fines generation (-106 µm) a notable increase occurred after 100 revolutions, and again after 2000 revolutions.

Due to the variation in the feed particle size analyses, the fines (-106µm) generated with each test is shown in Figure 33 together with that present in the initial feed sample. For blocks L1R9 and L1R11 (both 3 days water cooling) the absolute -106µm fraction appears to stabilize at 1000 revolutions. The fines generated with block L2R9 (higher tapping rate, 10 days water cooling) appears to be a strong function of the amount of fines present in the feed sample. The fines generated from block L2R11 (low tapping rate, 10 days water cooled) does not appear to stabilize, even after 2000 revolutions and is greater than that of any of the other blocks.

In order to compensate for the variation in the particle size distributions of the feed material, the product-to-feed ratios of the fines are shown in Figure 34. In this graph, a product-to-feed ratio of 1 would indicate no generation of additional fines during the test, while a product-to-feed ratio larger than 1 indicates that fines were generated in the tumble test.

Already from 200 revolutions and onwards, the more slowly tapped blocks L1R11 and L2R11 show more fines generation than the faster-tapped blocks L1R9 and L2R9. At 2000 revolutions the fines generated from block L1R11 (lower tapping rate, 3 days water cooled) is the most, with the least generated from block L2R9 (higher tapping rate, 10 days water cooled). The second best performer in terms of fines generation is block L1R9 (fast tapping, 3 days water cooled), with block L2R11 (low tapping rate, 10 days water cooled) rated as third best performer.

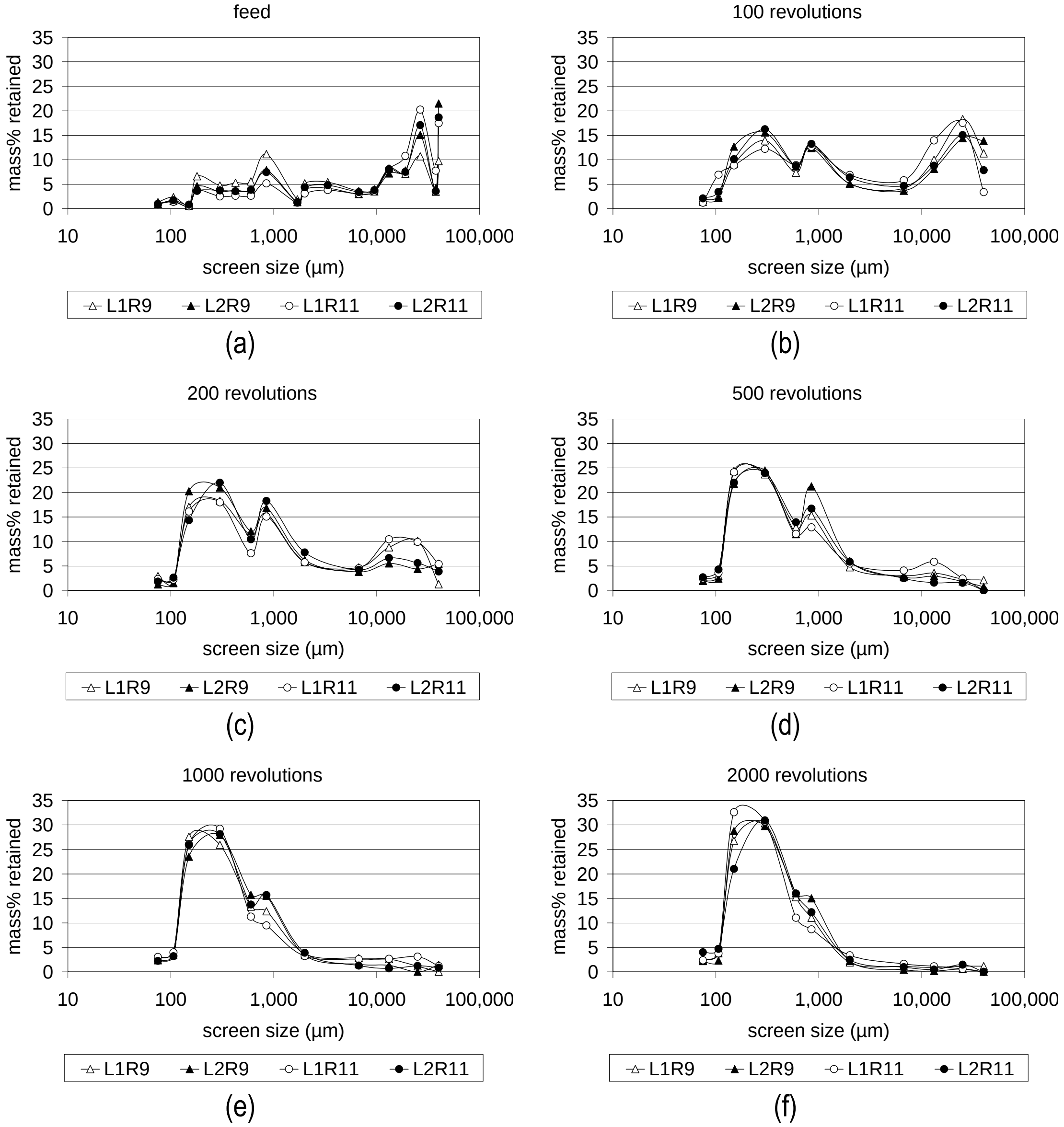

Figure 32 Particle size distributions of the tumble test feed and products.

For a given tapping rate, it is furthermore clear (Figure 34) that the blocks which were cooled for 10 days generated less fines during tumbling than those cooled under water for 3 days only.

The residual coarse fraction present in the product, together with that present in the feed of each tumble test, is shown in Figure 35. Similar to evaluation of fines generation, the variation in particle size distribution of the feed was compensated for by expressing the residual coarse in the feed relative to that in the product (Figure 36). In this graph a ratio of 1 would indicate that the coarse material (+850 µm fraction) in the product is equal to that in the feed; hence no breakdown. A feed-to-product ratio larger than 1 indicates that the coarse material in the feed is more than that in the product - hence breakdown of the coarse fraction (+850 μm) did occur.

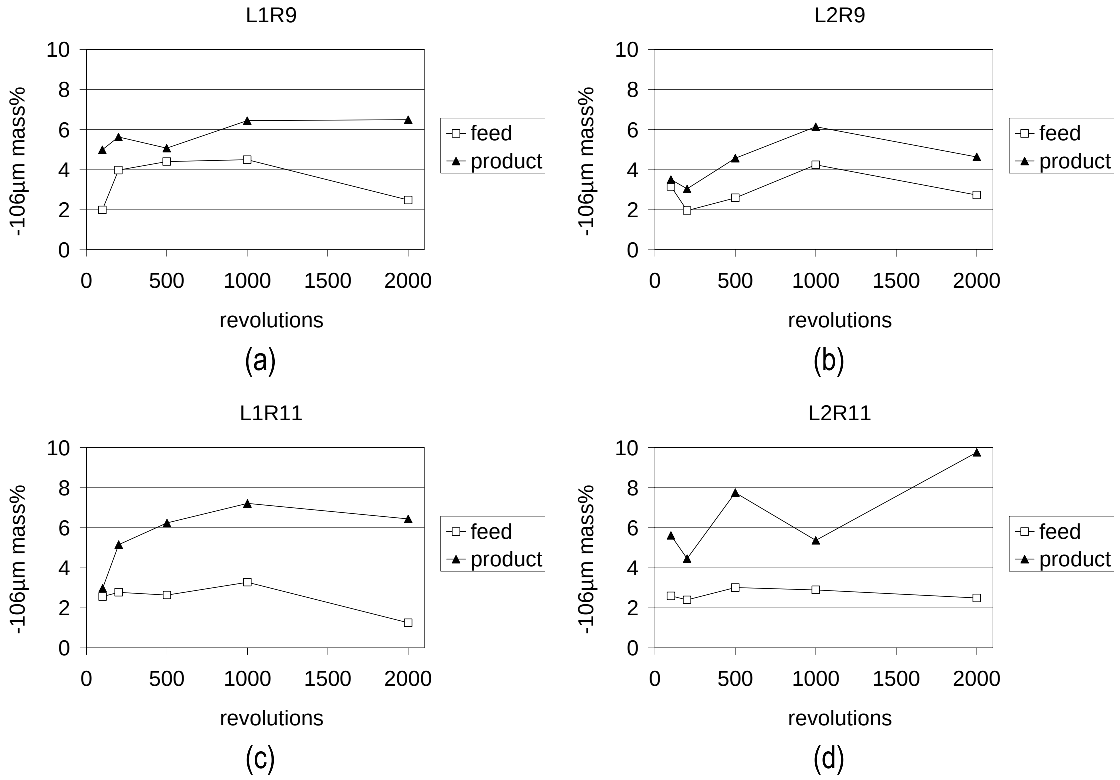

(a) (b)

(c) (d)

Figure 33 -106µm fraction (fines) generated with each tumbling test (solid markers). The fines present in the feed are shown by the open markers.

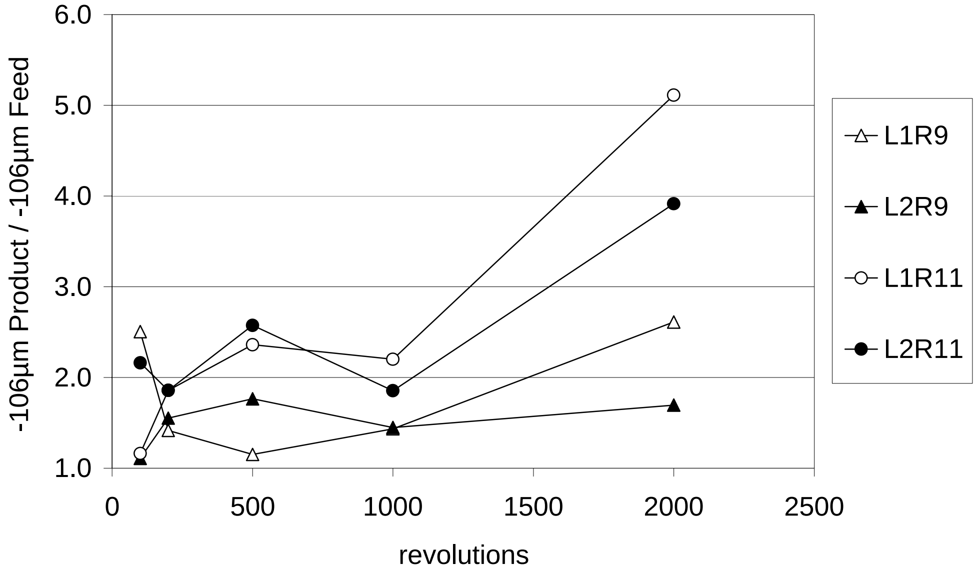

Figure 34 Ratio of -106 µm in the product to that in the feed of the tumbling tests. Circles denote low tapping rates and triangles high tapping rates. Solid symbols denote 10 days of water cooling while open symbols represent 3 days of water cooling.

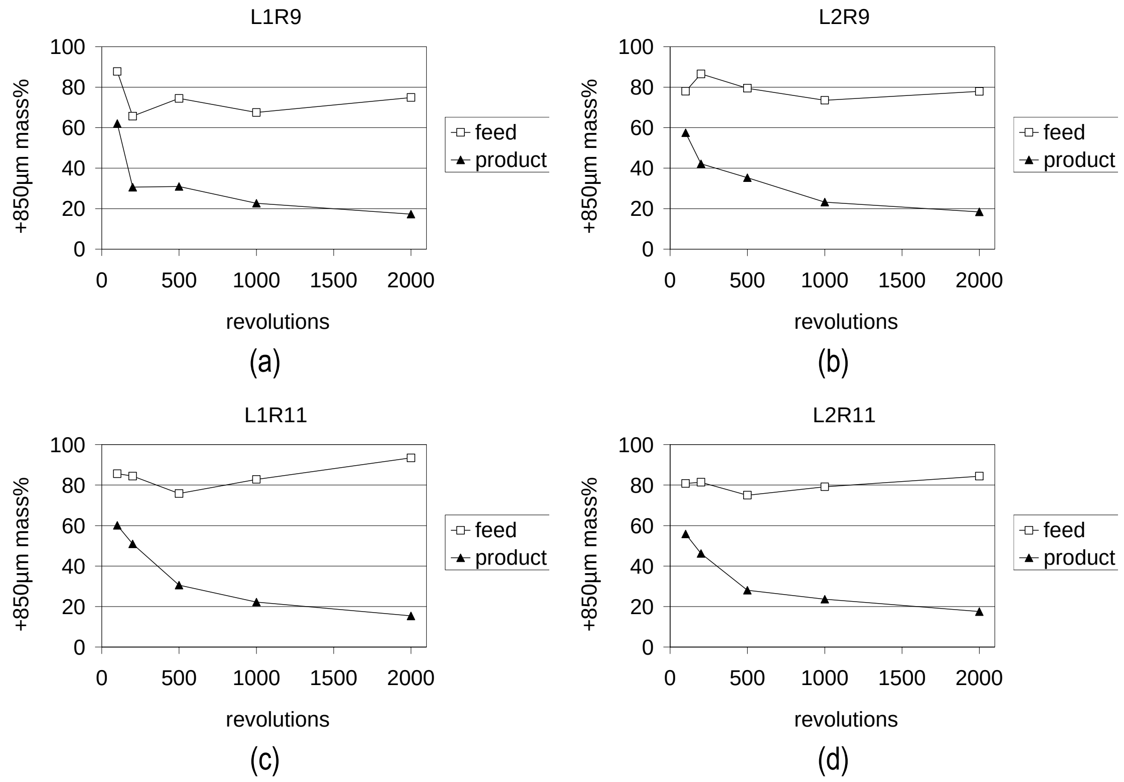

(a) (b) (c) (d)

Figure 35 The +850 µm fraction (residual coarse) remaining after each tumbling test (solid symbols). The coarse material present in the feed is shown by the open symbols.

Breakdown of the coarse material occurred with all four blocks from 100 revolutions and continued to 2000 revolutions (Figure 36). The initial breakdown (at 200 revolutions) is more for the faster-tapped blocks (L1R9 and L2R9) than for the more slowly tapped blocks. With further tumbling the breakdown slows down for the faster-tapped blocks compared to that of the more slowly tapped blocks.

The absolute values of the coarse material for all four blocks appears however to have stabilised from 1000 revolutions onwards between the four blocks (Table 8). The higher level of breakdown as implied by Figure 36 is attributed to the difference in feed particle size distribution – especially that of the coarser block L1R11 (Figure 31).

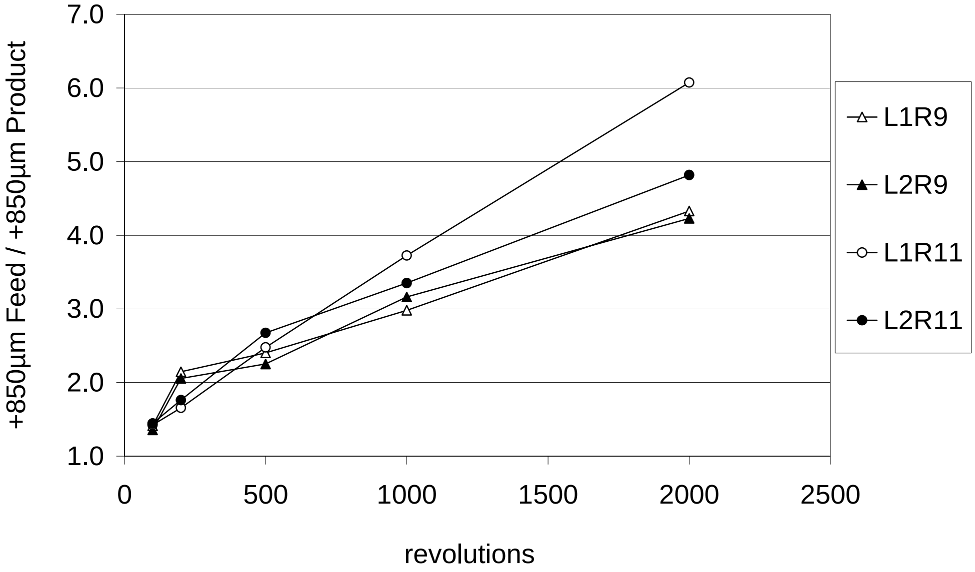

Figure 36 Ratio of the +850 µm in the product to that in the feed of the tumbling tests. Circles denote low tapping rates and triangles high tapping rates. Solid symbols denote 10 days of water cooling while open symbols represent 3 days of water cooling.

Table 8 Absolute values of the residual coarse fraction (+850 µm) of the tumbling products.

Revolutions	**100**	**200**	**500**	**1000**	**2000**
L1R9	62.04	30.59	30.96	22.64	17.30
L2R9	57.47	42.12	35.29	23.24	18.43
L1R11	60.13	50.97	30.61	22.24	15.39
L2R11	55.92	46.21	28.05	23.64	17.52
average	58.89	42.47	31.23	22.94	17.16
std. deviation	2.726	8.708	3.002	0.623	1.280

Based on these results, and assuming that the tumbling test is a simulation of material abrasion during handling the following is concluded:

- The effects of tapping rate and cooling history on the abrasion resistance of the slag are noticeable in the fines generation, and less so in the residual coarse fraction of the four blocks.

- The two blocks which were water cooled for 10 days generated less fines during extended handling (2000 revolutions, Figure 34) than their counterparts which were water cooled for 3 days only.

- The faster-tapped blocks outperformed their more slowly tapped counterparts in terms of limited fines generation (Figure 31).

Hence a faster-tapped block, cooled for 10 days yields the best abrasion resistance properties, while a more slowly tapped, insufficiently cooled block yields the poorest abrasion resistant properties. Increased water cooling of a more slowly tapped block mitigates the abrasion of a slowly tapped block to some extent.

3.4 Compression tests

3.4.1 Method

The objective with the compression tests was to simulate the milling action of the Loesche mill (Figure 37). Similar to the Loesche mill, the experimental set-up used for the compression tests utilised in-bed compression breakage principles where[27]

(i) The bed of particles shield a particle from secondary breakage (i.e. the further breakdown of particles which formed from the mother particle during primary breakage);

(ii) The limited force applied limits secondary breakage, and

(iii) The porosity of the bed allows particles and fragments to "hide" from the applied force.

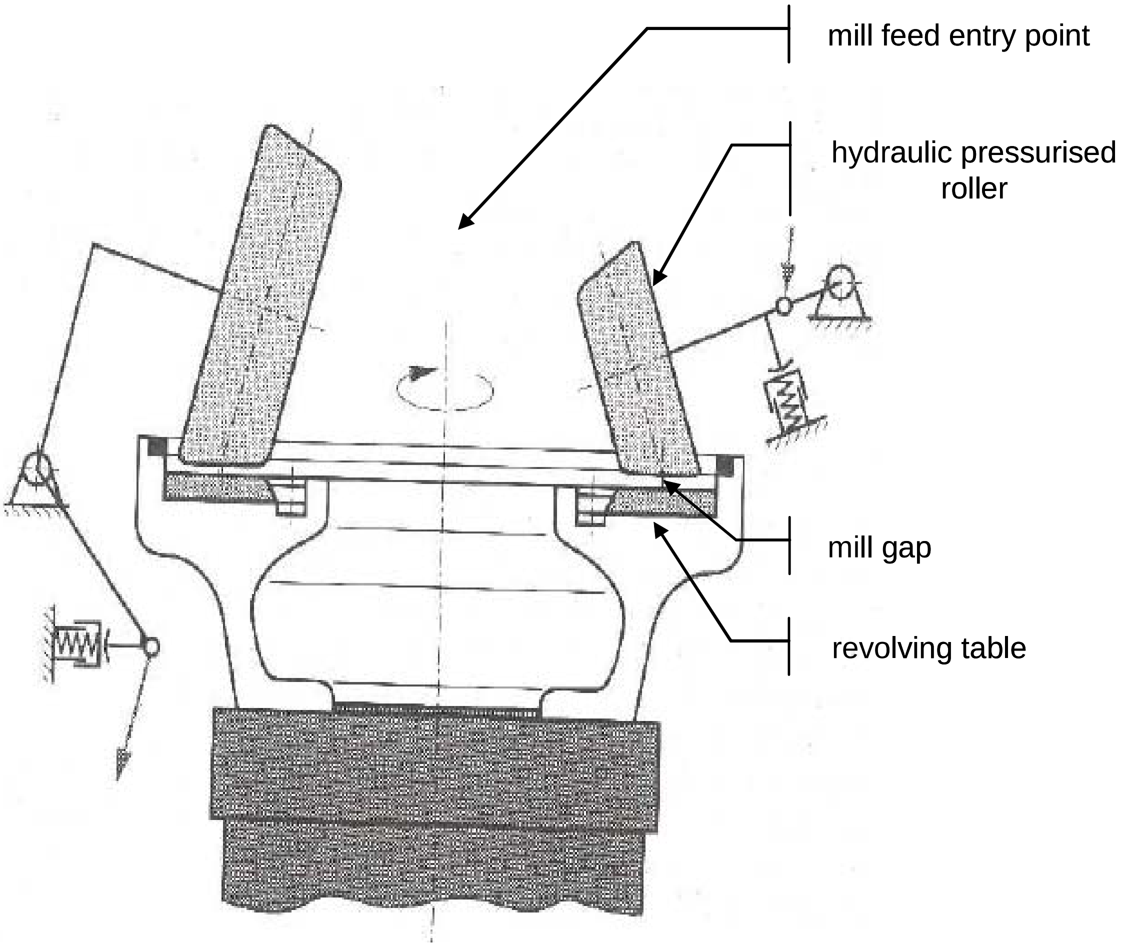

Figure 37 Sketch of a typical Loesche mill[28].

The experimental compression equipment (Figure 38) consisted of a steel sample container with inner diameter of 140 mm. Compression was applied in a vertical direction with an anvil pressing down into the sample container. On compression the anvil travelled 20 mm from its starting position, recording distance and applied force (recorded in tons) against time (Figure 39(a)). The compression force was calculated from the product of the "ton force" and the gravity constant – assumed to be 9.81 N/kg. The total compression energy was calculated by integrating the area below the distance-force curve. To determine the compression energy exerted onto the slag (Figure 39(b)), the compression energy stored in the machine was determined and deducted from the total compression energy. (That is, elastic deformation of the testing machine absorbs some energy which is not transferred to the sample.)

The energy stored in the machine itself is calculated from equation (3), where k is a constant quantifying the machine stiffness. The machine stiffness was hence determined from a series of sample-free compression tests. By inserting the force and energy parameters into equation (3) the machine stiffness was calculated as 314.4 ±21.5 kN/m (at a 95% confidence level).

$$E_{machine} = \frac{1}{2}\frac{F^2}{k} \tag{3}$$

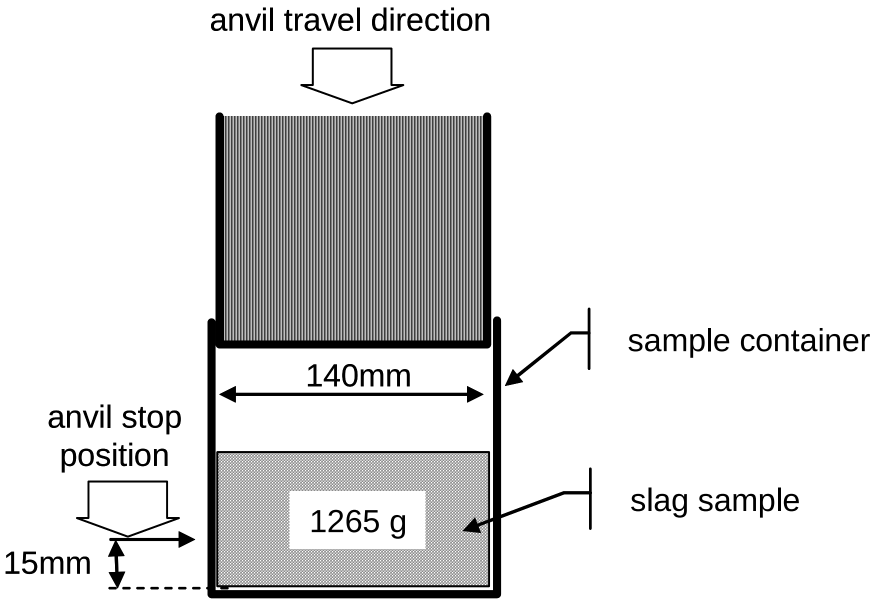

Figure 38 Schematic depiction of the experimental set-up for the compression testwork.

The sample container was filled with a 1265 g sample, corresponding to a sample height of approximately 35 mm - varying slightly according to sample heap density (due to varying particle size distributions). The anvil travelled a maximum of 20 mm downwards, aiming to compress the sample to 15 mm, which is similar to the gap setting between the Loesche mill table and roller. Since the maximum force was kept constant for each test – averaging 198.6 kN within a range of 194.5 and 203.3 kN (Figure 40(b)) – the travel distances ranged from 7.7 to 15 mm with an average of 9.8 mm (Figure 40(a)). On completion of a test, the -850 µm size fraction was removed from the sample (by screening) and replaced with an equal mass of fresh material and the test repeated. Removing the -850µm product fraction from the sample simulates the process flow of the plant (Figure 1) where the finer fraction is removed by screening in a closed loop with the Loesche mill. Six compression runs were conducted with each sample.

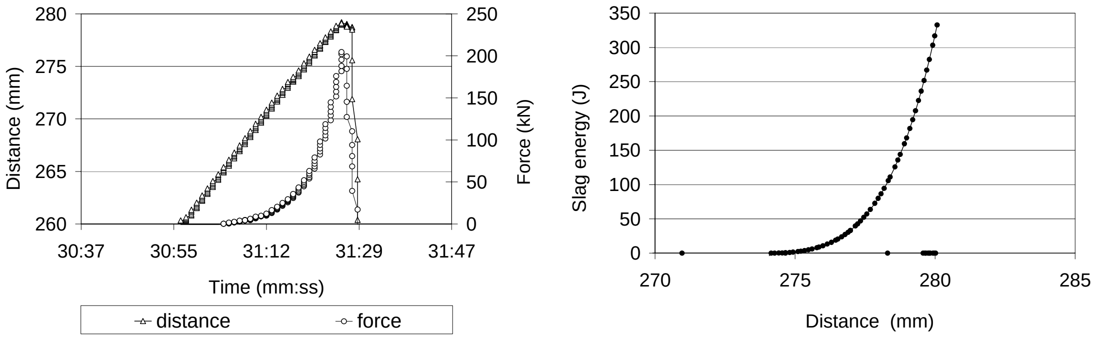

(a) (b)

Figure 39 Example of (a) recorded distance and force and (b) compression energy as calculated during the compression tests.

The compression distance for sample L1R9 was significantly larger than that for the other three samples. This could be attributed to the smaller particle sizes of sample L1R9 (Figure 31), leading to a more compressible bed compared with that of the other three samples.

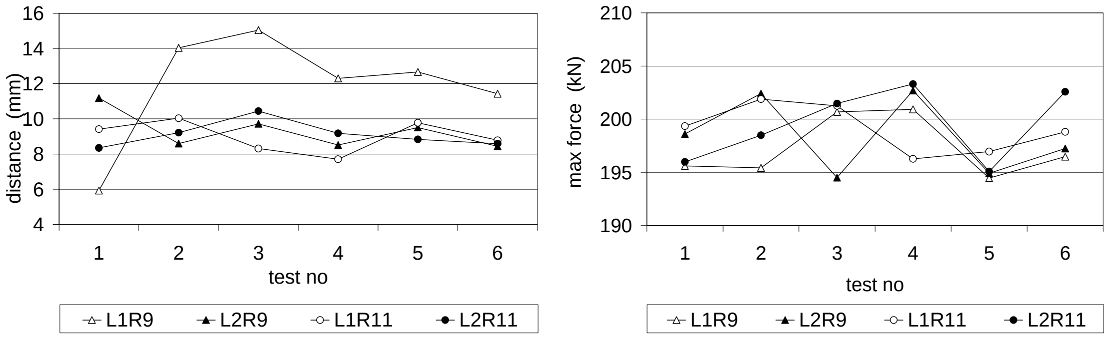

(a) (b)

Figure 40. Distance (a) and maximum force (b) per test as recorded during the compression tests.

The specific energy input for each run (measured in kJ per total kg sample mass) is shown in Figure 41. Due to the further distance recorded for sample L1R9, the specific energy for the latter is higher than that of the others.

The typical energy consumption in the industrial scale Loesche mill is 0.4 to 0.8 kWh/t slag in comparison with 0.11 kWh/t slag (0.4 kJ/kg sample) of the experimental work.

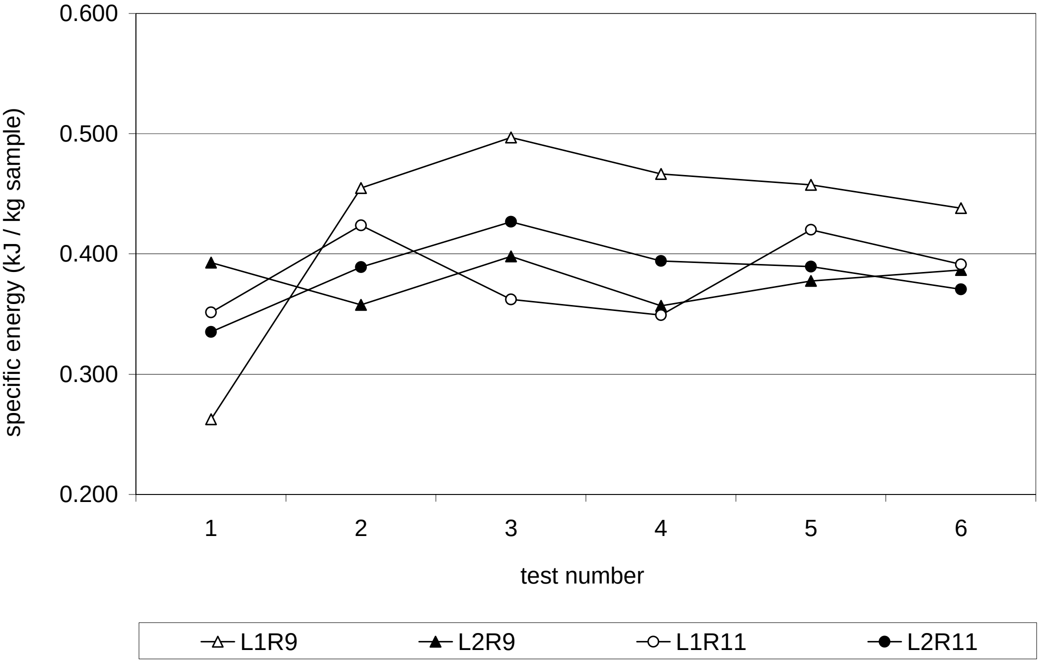

Figure 41. Specific energy exerted on the samples during the compression tests.

3.4.2 Results

The absolute mass percentage fines generated with each compression run is relatively constant from the second to the sixth run for all four blocks, Figure 42(a). The specific energy (measured in kJ per mass%-106µm) also appears to be relatively constant over the second to sixth runs for all four blocks, Figure 42(b).

The absolute mass% residual +850 µm is consequently lower for the two slower tapped blocks L1R11 and L2R11 from run 3 onwards (Figure 43).

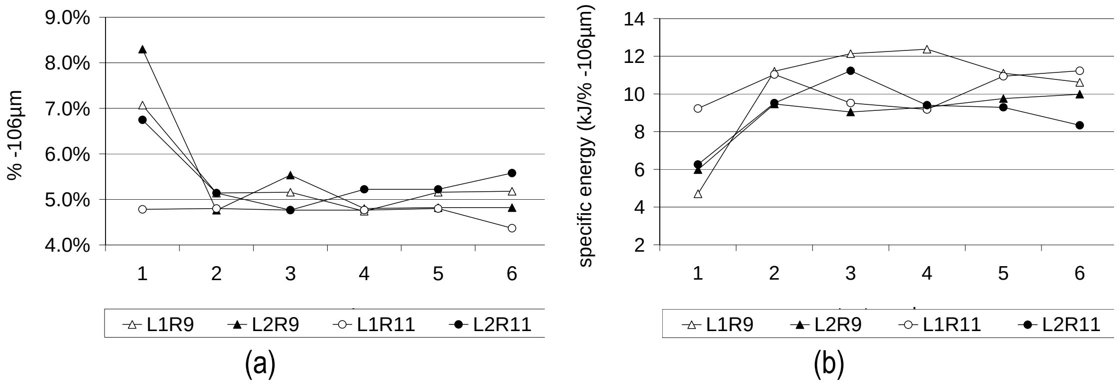

(a) (b)

Figure 42 (a) Amount of fines generated with the 1st to 6th run of the compression test series for the four blocks. (b) Specific energy (kJ per mass% -106 µm) per compression run for the four blocks.

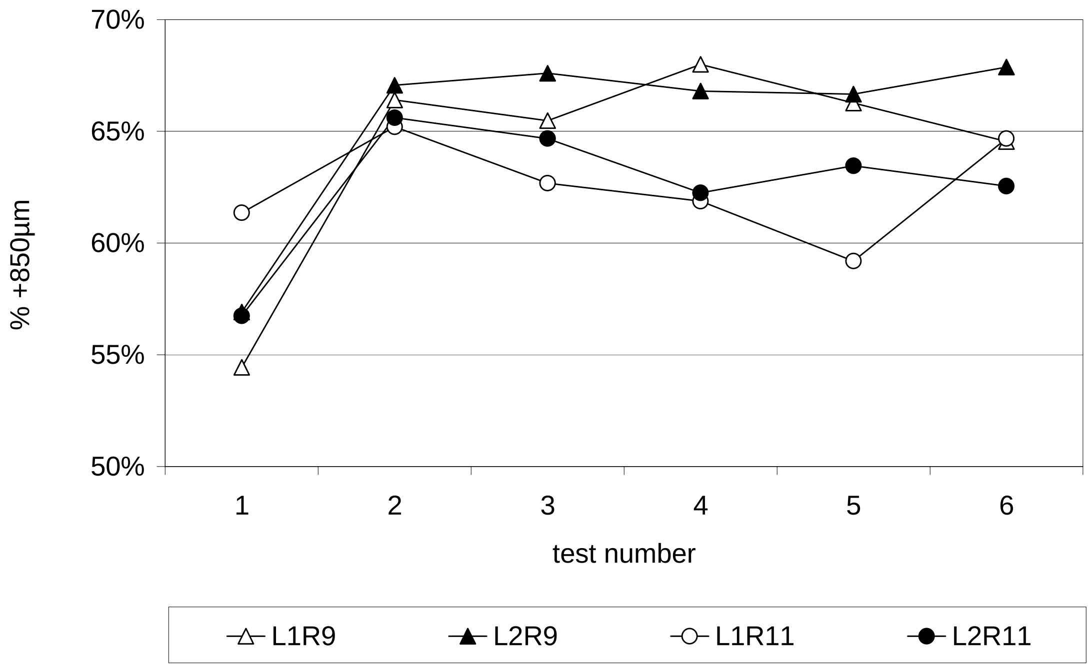

Figure 43 (a) Residual +850 µm mass% from the 1st to 6th test of the compression test series for the four blocks; (b) Specific energy (kJ per mass% +850 µm) per compression run for the four blocks.

Averages over the last 3 runs of each test, for both the fine and coarse fractions, are given in Table 9 and are graphically represented in Figure 44 and Figure 45 (variations are calculated for a 95% confidence interval).

The absolute value for fines generated for the four blocks overlap to a large extent; as does the specific energy requirement (Figure 44). The variation in the specific energy requirement for fines generation is relatively large for the L1 blocks which were water cooled for 3 days only.

The residual coarse mass% of the R9 blocks which were tapped faster is higher than that of the more slowly tapped blocks. This is in agreement with the results from Part 1. Block L1R11 (more slowly tapped and water cooled for 3 days only) showed a large variation in its residual coarse fraction (Figure 45). The specific energy required per mass unit +850 µm overlaps largely, while block L1R11 continues with the tendency to have the largest variation in its particle size distribution.

Table 9 Average numbers for the last 3 compression tests ran for each block, including 95% confidence intervals.

	% -106 µm	Specific energy (kJ / %-106 µm)	% +850 µm
L1R9	5.03 ±0.28	11.36 ±1.027	66.3 ±1.95
L2R9	4.81 ±0.01	9.68 ±0.400	67.1 ±0.75
L1R11	4.64 ±0.27	10.45 ±1.255	61.9 ±3.10
L2R11	5.34 ±0.23	9.01 ±0.660	62.8 ±0.71

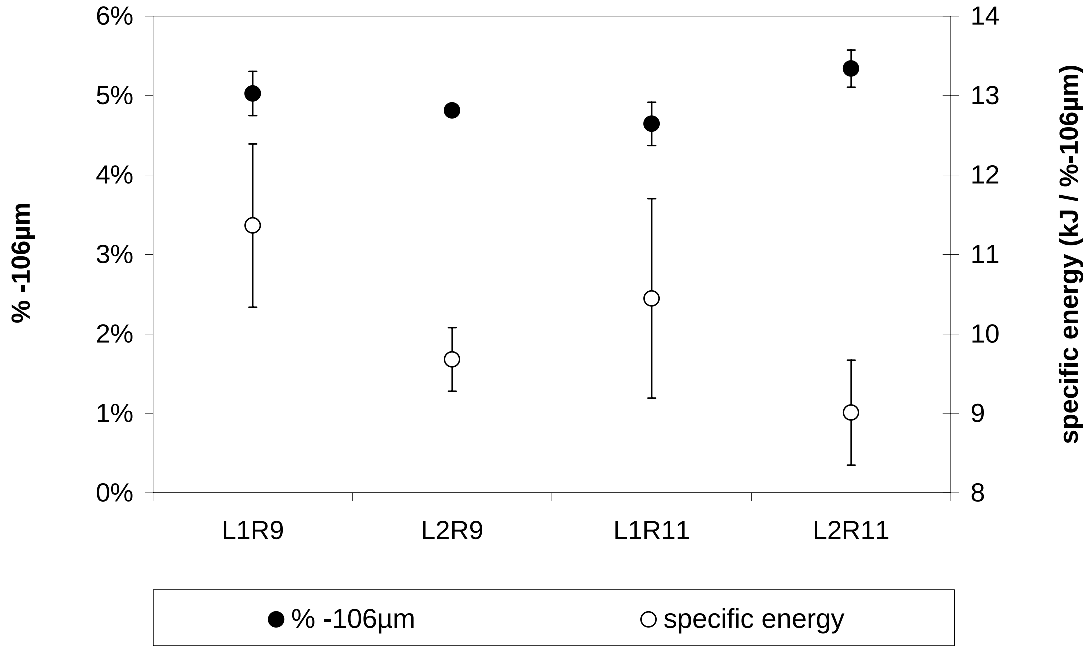

Figure 44 Average % -106 µm and specific energy in kJ/% -106 µm per compression test for each of the four blocks. (Error bars showing a 95% confidence interval).

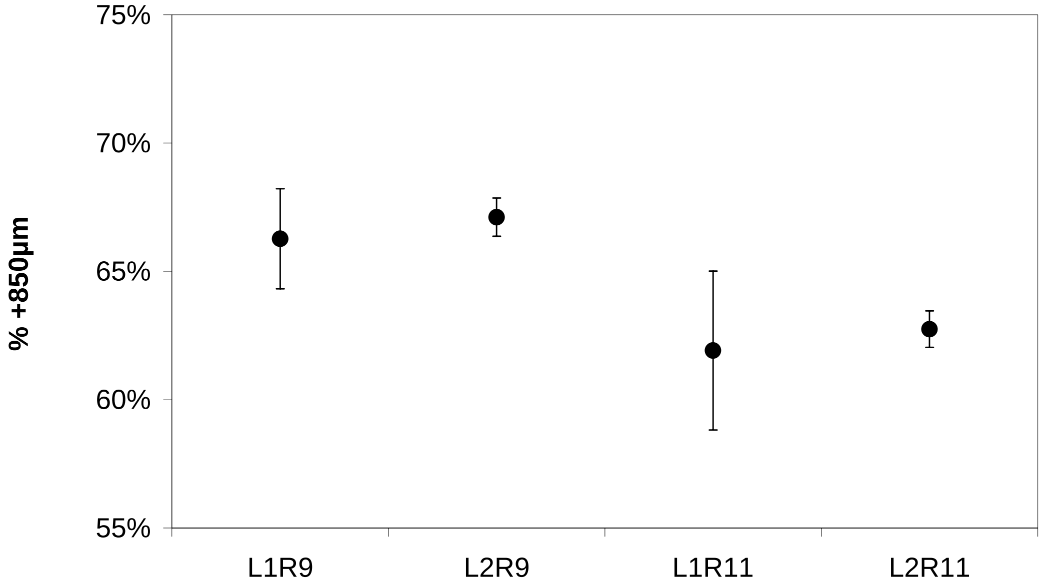

Figure 45 Average % +850 µm per compression test for each of the four blocks. (Error bars showing a 95% confidence interval).

Despite the larger travel distance imposed on the sample from block L1R9 (and hence the larger applied specific energy) the particle size distribution of its compression product does not differ significantly from those of the other three blocks. This is likely attributable to the “hiding” opportunity the slag has under the inter particle (or in-bed) compression conditions characteristic of this compression method. This implies that the particle size distribution of the mill product is primarily a function of the feed size distribution, which in turn appears to be a function of the tapping rate and cooling history (Figure 31) – and not the energy applied within the mill.

Block L1R11 which tapped more slowly and was water-cooled for 3 days showed a larger variation in particle size distribution relatively to the other three blocks. On the other hand, block L2R9 (tapped faster and cooled for 10 days under water) consistently showed small variations in its particle size distribution. The small variations in especially the coarser fractions of the R11 blocks (10 days water cooled) combined with the similar particle size distributions of these fully water cooled blocks (as per Figure 31) – despite their differing tapping rates - supports a line of reasoning that sufficient water cooling "homogenises" the particle size distribution of the block during subsequent comminution.

3.5 Slag composition and mineralogy

A drill core which was prepared from one of the pilot-campaign slag blocks, and samples from a slag block from the industrial plant, were examined by scanning electron microscopy. The objective was to test possible relationships between the slag block microstructure and its crushing behaviour. At least three microstructural links are possible: (i) the role of silicates, (ii) the karrooite (M_3O_5) grain size, and (iii) cracking by incipient low-temperature oxidation.

As discussed in section 1, silica and calcia are not soluble in the karrooite matrix phase, and form silicates which solidify at a lower temperature than the karrooite. During solidification of the karrooite, the silica and calcium oxide (and also some alumina, titanium oxide, iron oxide and manganese oxide) hence form a separate, low-melting phase which is expected to collect within the solidified matrix. Depending on the nature of the solidification front, the silicate may collect in the middle of the solidifying block, or it may be present between the karrooite dendrites. If the latter, the presence of the silicates can be expected to affect the size reduction behaviour, by means of fracture through the silicates or between the silicates and the karrooite (in line with the effect of silica content on fines generation, as observed from the pilot-campaign slags).

Given that cleavage of the karrooite grains is the fracture mechanism, grain size and grain shape are important. Visual observation of polished sections of slag indicates that individual grains are needlelike in shape, up to several millimetres long, and less than a millimetre in width. This is comparable with the required grain size for the chloride slag product, which is between 106 µm and 850 µm.

Finally, as mentioned earlier, low-temperature oxidation can cause fine slag fragments to form (triggered by the volume change associated with the appearance of the M_6O_{11} phase[7]).

3.5.1 Method

Block 60 produced during the Campaign 9 pilot plant trials were horizontally core drilled as shown in Figure 46. The outer end of the core shows the typical denser structure, while porosity is apparent in the centre portion of the core. Block 60 had a tapping rate of 396 kg/min (the third highest tapping rate of the taps discussed in Part 1); had a mass of 1,557 kg and was continuously water cooled. The tap analysis of this block is shown in Table 10.

Figure 46 Cross section of block 60 showing the horizontal groove where the drill core was removed. The block surface is apparent from the rusty coloured area in the upper left hand corner of the photo.

Table 10 Tap composition of block 60 (mass percentages; XRF)

FeO	TiO_2	Al_2O_3	CaO	Cr_2O_3	MgO	MnO	SiO_2	V_2O_5
9.78	87.57	0.81	0.20	0.11	1.49	1.21	1.28	0.48

Polished sections were prepared from three positions along the drill core. These were at the surface of the block (where it had been in contact with the mould), halfway between the surface and the centre, and at the centre of the block. The sections were sputter-coated with gold, and examined by scanning electron microscopy, using back-scattered electron imaging to yield atomic-number contrast. Micro-analyses were performed by energy-dispersive spectroscopy (EDS), in the scanning electron microscope. At least four regions were analysed per phase or area, and 95% confidence intervals on the mean composition calculated. Similar samples were obtained from the industrial plant; plant personnel collected samples from a single block, for regions at the surface of the slag block, within the block interior (but away from the centre), and at the centre (at the position of final solidification, as indicated by noticeably greater porosity).

Crushed plant slag samples were also examined. These were examined without mounting, by simply pouring some of the slag over conductive carbon tape, and then sputter-coating the adhering particles with gold.

To limit the size of the interaction volume an acceleration voltage of 12 kV was used.

3.5.2 Results

3.5.2.1 **Slag block microstructure**

The observed microstructure for the drill core was similar for all three samples (which spanned the distance from the slag block surface to its centre) with the exception of the outer surface, which showed a chill zone – which also displayed substantial oxidation – next to the mould surface. Figure 47 shows a chill zone, at low and higher magnifications. The presence of a substantial amount of rutile indicates that oxidation of the slag had taken place, during or after solidification: if some of the Ti_2O_3 in the slag is oxidised, the slag composition departs from M_3O_5 stoichiometry; specifically, the slag contains more TiO_2 than M_3O_5 stoichiometry would require, with the result that rutile would form as primary phase during solidification. Such a structure could also arise by oxidation of the slag after solidification. Approximately 3 mm away from the chilled surface, no free rutile was observed in the microstructure, which then consisted of the dominant karrooite phase, with some silicates. Fine cracking of the karrooite was visible, probably as a result of some low-temperature oxidation. The lower-magnification micrograph (left hand side of Figure 48) shows the karrooite grains to be delineated by the silicate phases. Two types of silicate phase were observed; one (S_1) appeared darker in the back-scattered electron image (indicative of a lower average atomic number). Both S_1 and S_2 contained an internal structure of secondary phases. These phases could not be identified, since they were too small to analyse by EDS.

The same general features were observed in the other two samples: rutile was present, apparently as a solidification product, in both the "halfway" and "centre" samples. The karrooite grain size is not readily apparent, but – based on delineation of the karrooite grains by the silicate phases – there is not a major difference in the grain size or shape for the different positions within the block. In all cases, the grains appeared elongated in the polished sections, up to 0.5 mm long, and typically 100 µm or less across.

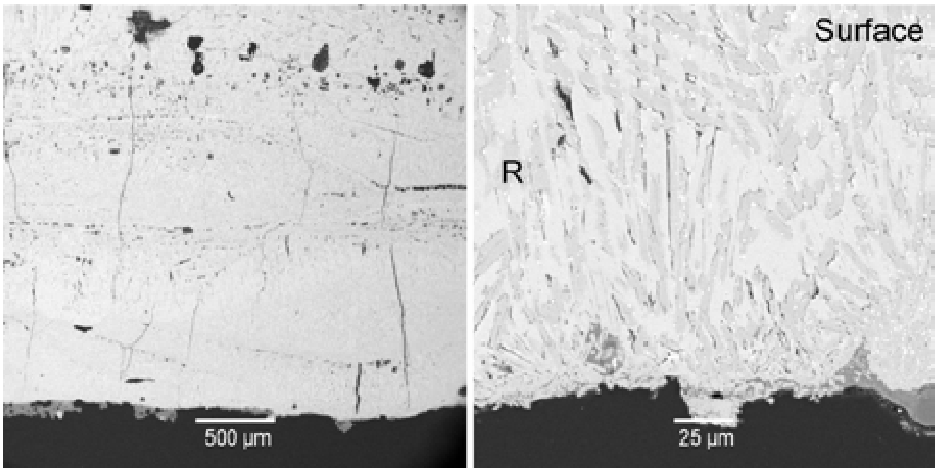

Figure 47 Microstructure of the chill zone in the pilot-plant slag block, next to the mould. The outer surface is at the bottom of both images. The higher-magnification image at right shows that this region largely consists of two phases; the darker phase (marked "R") was found to be TiO_2 (rutile or anatase).

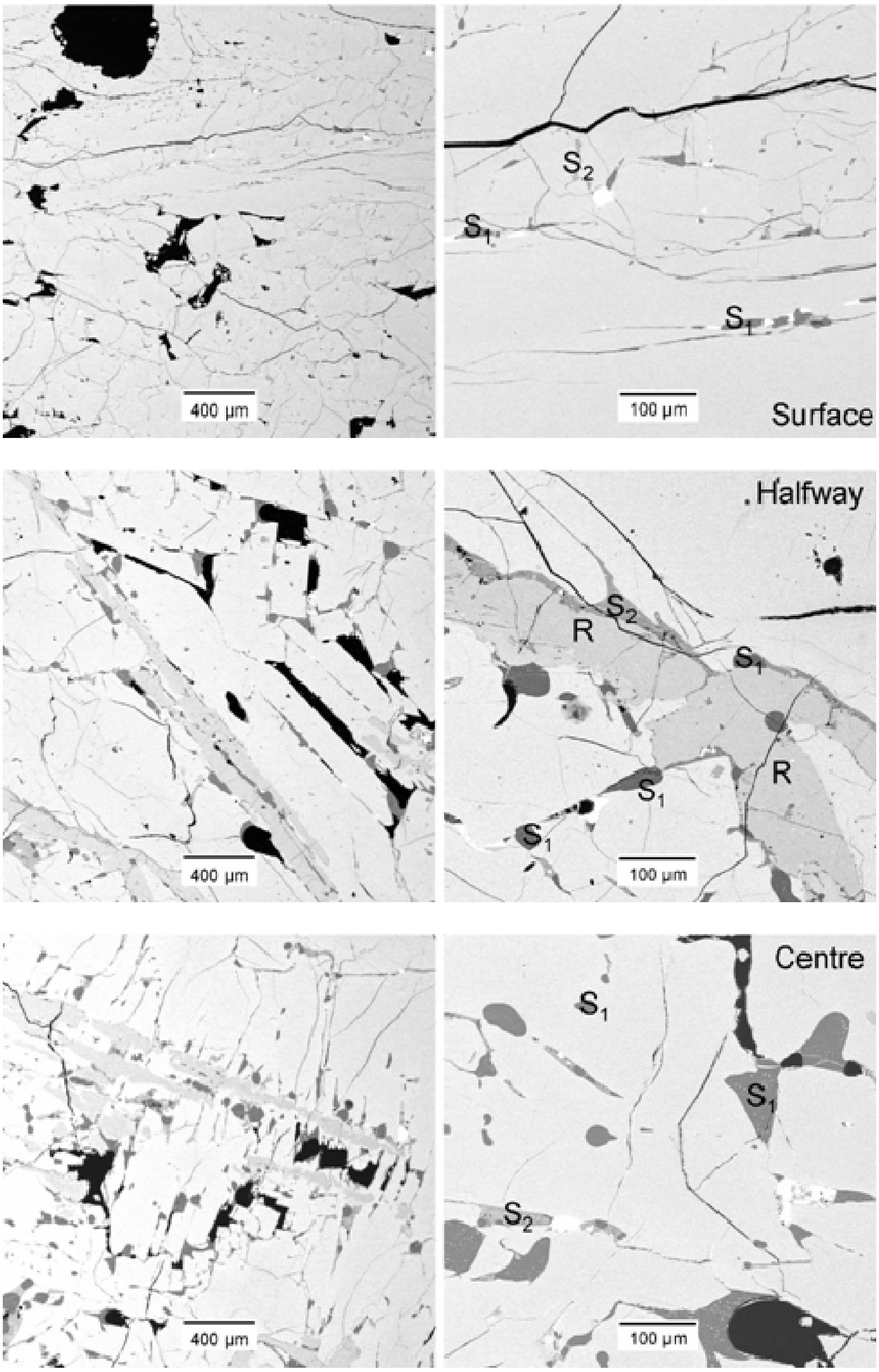

Figure 48 Typical microstructures found within the pilot-plant slag block, near the surface of the slag block, but outside the oxidised zone (top two images), halfway between the surface and the centre (middle two images), and at the centre (bottom two images). The light-gray matrix phase is karrooite (M_3O_5), the black lines are cracks, larger black areas are pores, dark grey areas are silicate phases (S_1 and S_2), and the phase with intermediate brightness is TiO_2 (likely rutile; indicated with R).

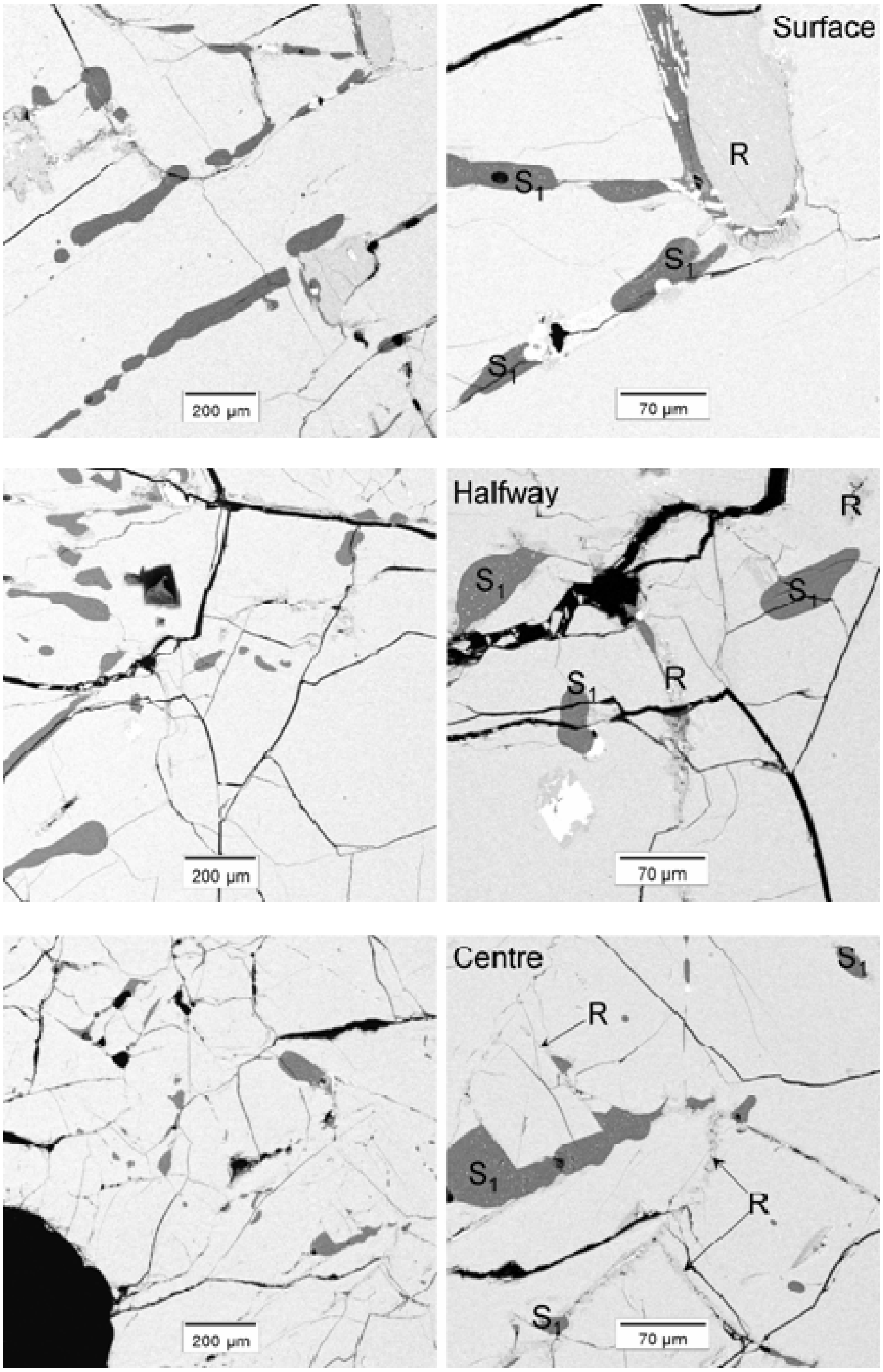

Figure 49 Typical microstructures found within the industrial-plant slag block, near the surface of the slag block, (top two images), within the body of the slag block (middle two images), and at the centre (bottom two images). Phase identification is as for the images of the pilot-plant slag block.

Table 11 Average compositions (with 95% confidence intervals on average values), as found by EDS. Compositions are in mass percentages. For the karrooite phase, the Ti_2O_3 content was calculated by assuming that M_3O_5 stoichiometry holds. For the area analyses and silicate analyses, all titanium is expressed as TiO_2.

Karrooite (pilot-plant slag):

Position	TiO_2	Ti_2O_3	FeO	MnO	MgO	Al_2O_3
Surface	49.6±2.0	37.7±3.9	8.9±1.9	0.9±0.4	1.9±0.3	0.9±0.2
Halfway	55.0±1.4	27.3±2.7	13.0±0.7	2.1±0.4	1.7±0.4	0.9±0.2
Centre	55.3±1.8	26.6±3.4	13.5±1.5	2.0±0.6	1.7±0.2	0.9±0.1

Darker silicate (labelled "S1" in micrographs):

Position	SiO_2	TiO_2	CaO	K_2O	Al_2O_3	FeO	MnO	MgO
Pilot plant slag								
Surface	76.2±5.2	9.8±3.3	3.7±1.2	2.1±0.1	3.4±0.2	2.8±1.3	1.8±0.7	0.1±0.1
Halfway	81.9±1.3	7.1±0.8	2.6±0.4	2.5±0.1	3.7±0.2	1.5±0.3	0.8±0.4	0.0±0.1
Centre	78.6±5.7	9.1±3.6	3.1±1.7	2.3±0.5	3.7±0.3	2.1±0.8	1.0±0.4	0.1±0.1
Industrial slag								
Surface	82.5±1.1	7.6±0.9	2.3±0.5	2.7±0.2	3.7±0.2	0.8±0.6	0.3±0.3	0.1±0.1
Halfway	82.1±0.8	8.4±0.5	2.0±0.9	2.8±0.5	3.4±0.2	1.0±0.5	0.2±0.2	0.1±0.1
Centre	79.0±1.7	10.4±1.1	2.1±0.4	2.9±0.4	3.4±0.4	1.4±0.8	0.7±0.4	0.1±0.1

Brighter silicate ("S2" in micrographs): Only found in pilot-plant slag

Position	SiO_2	TiO_2	CaO	K_2O	Al_2O_3	FeO	MnO	MgO
Surface	38.1±5.6	33.1±6.9	20.3±3.2	0.6±0.3	1.6±0.8	1.7±3.0	4.4±2.9	0.2±0.1
Halfway	48.2±9.4	19.4±11.7	18.2±2.8	0.9±0.3	5.3±2.1	2.1±1.0	4.9±3.0	0.9±1.0
Centre	45.4±8.4	20.1±13.7	17.2±4.3	0.8±0.5	4.8±1.7	3.5±1.4	7.1±6.1	1.0±2.0

Average of phases (area analyses):

Position	SiO_2	TiO_2	CaO	K_2O	Al_2O_3	FeO	MnO	MgO
Pilot plant slag								
Surface	1.3±0.2	87.4±0.8	0.1±0.2	0.1±0.1	0.8±0.1	7.9±1.1	1.1±0.6	1.2±0.1
Halfway	3.2±1.4	81.1±2.5	0.4±0.4	0.0±0.1	1.0±0.3	10.7±1.3	2.4±0.7	1.3±0.1
Centre	3.3±1.4	80.1±4.2	0.4±0.3	0.0±0.1	0.9±0.2	11.3±2.3	2.8±1.2	1.2±0.3
Industrial slag								
Surface	2.7±1.6	83.8±3.1	0.1±0.2	0.0±0.1	1.0±0.2	9.1±1.9	2.3±0.7	0.8±0.1
Halfway	2.5±2.8	85.4±4.8	0.1±0.3	0.1±0.2	1.2±0.2	7.1±2.2	2.7±0.7	0.9±0.4
Centre	1.9±0.3	86.1±3.4	0.0±0.1	0.1±0.2	1.2±0.3	7.3±2.2	2.5±1.2	0.9±0.2

The two silicate phase regions were observed throughout. Both contained a substructure of finer phases (which could not be analysed, because of their small size). The two types of silicates were distinguished on the basis of their appearance in the back-scattered electron images.

The observed internal cracking has the morphology of the cracking caused by low-temperature oxidation (M_6O_{11} formation).

The microstructures of the slag samples from the industrial plant were remarkably similar to those from the pilot plant. The only difference was that the silicate phase S_2 was not present.

A noticeable feature of the microstructures is that the internal cracks are often associated with the silicate phases and with the rutile grains (the silicates and rutile are present in the same region of the microstructure, namely where final solidification occurred between the karrooite grains). As noted below, this association was confirmed by the presence of silicate phases on the surface of crushed slag. This also supports the plant observation (discussed in Part 1) that both the silica content and the degree of oxidation during tapping (or tapping rate) affect fines formation. (The significance of oxidation is that rutile is present as a result of oxidation during tapping.)

3.5.2.2 **Micro-analyses**

The analyses found by EDS are summarised in Table 11. In the case of the pilot-plant slag, the composition is different for the sample from the block surface, but the average compositions and those of the individual phases are the same (or at least not significantly different) for the other two positions. This indicates that little macro segregation takes place during solidification, and also that the silicate phases are trapped between the karrooite grains as solidification progresses: there is no significant rejection of the silicates to the centre of the slag block. (The obvious exception to these observations is the near-surface chill region, where the titanium content of the karrooite is higher, and the silicate content is lower.) The same observations were made for the samples from the industrial plant.

3.5.2.3 **Crushed slag**

The main microstructural features observed from the drill-core (pilot-plant) and industrial samples are elongated karrooite grains (of similar size throughout), silicates present between the karrooite grains, and microcracking. Microscopic examination of the crushed chloride-grade slag (between 106 μm and 850 μm in size) indicates that the silicates do affect the crushing behaviour significantly for this size fraction. This conclusion is based on the observation that silicates are present on the surfaces of the crushed slag. Examples are shown in Figure 50. Each of these figures shows a pair of back-scattered electron images (BEI) and secondary electron images (SEI) of the same slag particles. The secondary electron images show particle shape, whereas contrast in the back-scattered electron images arises from both shape (orientation) and composition. Where dark patches are present in the back-scattered electron images, these indicate the presence of silicates. Micro-analysis shows these patches to have the same composition as silicate phase S_1, as revealed by Table 12 (note specifically the similar levels of calcium, potassium and aluminium). This means that these silica-containing regions on the surface are most unlikely to be contaminants which were transferred to the particles during crushing, but rather are a feature of the slag itself.

The high concentration of silicates on the particle surfaces does indicate a significant effect of the silicates on crushing behaviour, when the slag is crushed to the chloride-grade size. (Note that, while only two examples are shown below, the association of silicates with the surfaces of crushed chloride-grade particles was found commonly; more examples are given in Appendix 5.3).

Table 12 Micro-analyses of dark regions (silicates) identified in crushed slag (mass percentages)

	SiO_2	TiO_2	CaO	K_2O	Al_2O_3	FeO	MnO	MgO
CP slag	73.0±7.3	12.2±3.4	2.2±0.9	2.2±0.5	3.6±0.8	5.1±3.8	1.6±1.2	0.1±0.1
Fine slag	73.5±8.3	13.8±5.9	1.7±0.5	2.0±0.7	3.6±0.4	4.7±2.4	0.7±0.4	0.1±0.1

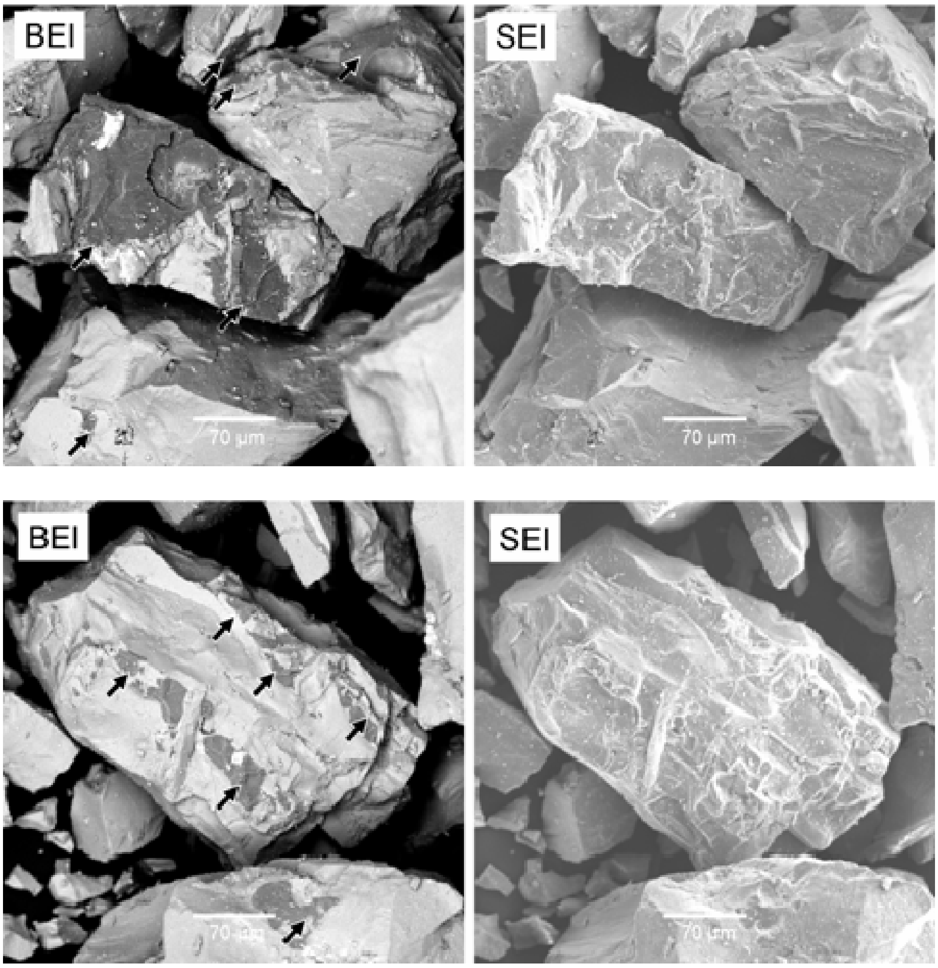

Figure 50 Pairs of images of the same particles of chloride-grade crushed slag. Arrowed black patches in the back-scattered electron images (BEI) at left indicate silicates. The secondary electron images (SEI) at right show the particle morphologies.

In contrast, the smaller, fine-grade slag particles do not show such an obvious association between silicates and particle surfaces (fracture surfaces). The smaller size and irregular shape (often apparently flakelike) of the sulphate-grade slag particles made it more difficult to identify silicate phases (by scanning electron microscopy). In all cases, identification of silicates was based on both brightness in the back-scattered electron image, and microanalysis by EDS. Examples of such silicate-containing particles are shown in Figure 51. As these examples illustrate, the silicate particles were generally found as liberated particles; the table of EDS analyses demonstrates that their compositions also agree with that of silicate S_1 in the microstructure. Note also that many of the crushed slag particles are much smaller than the silicate particles. It hence appears unlikely that the formation of these fine particles were affected by the presence of the silicates.

The visual observations in Figure 51 are confirmed by fractional chemical analyses done on composite industrial samples (shown in Figure 52). The oxides present in the glass phase increase markedly for particle sizes below 250 µm, whereas the same does not happen for Cr_2O_3, V_2O_5, and MgO, Figure 52(b). Note that chromium, vanadium and magnesium report to the karrooite (M_3O_5) phase, and not to the silicates. MnO does show a slight increase towards smaller particles sizes – likely due to a small portion of MnO reporting to the glass phase as mentioned earlier.

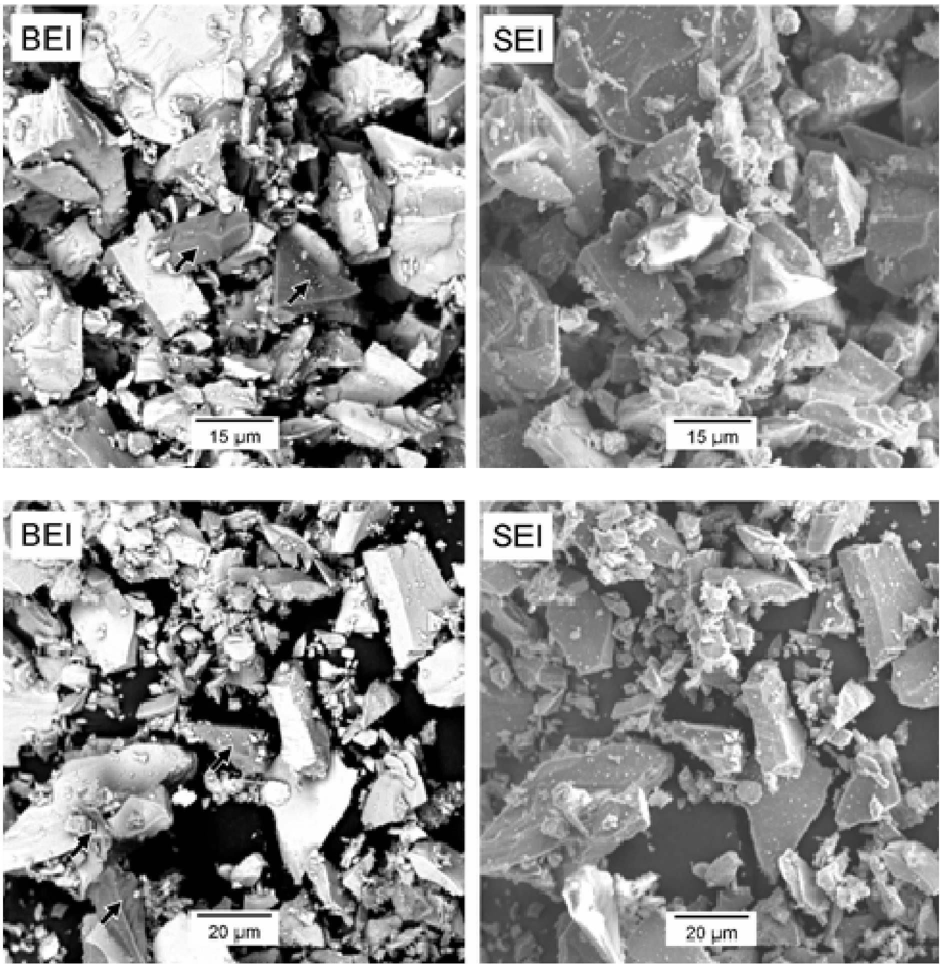

Figure 51 Pairs of images of the same particles of fine-grade crushed slag. Arrowed darker particles in the back-scattered electron images (BEI) at left indicate silicates. The secondary electron images (SEI) at right show the particle morphologies.

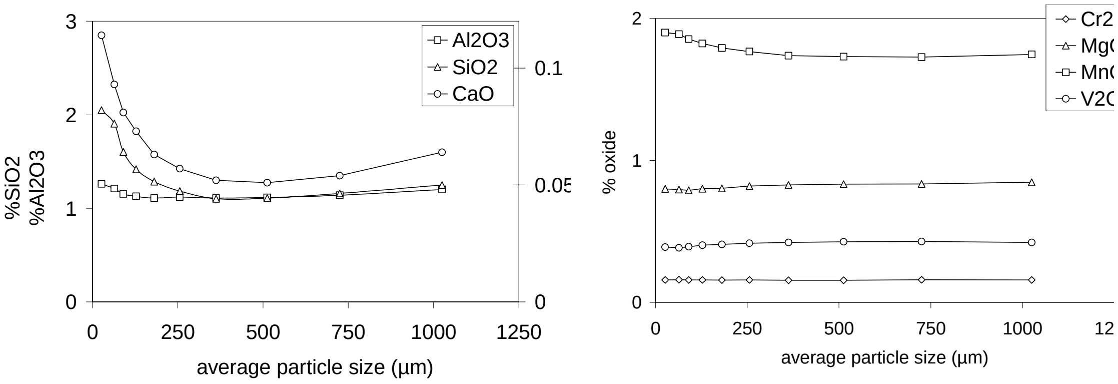

(a) (b)

Figure 52 %Oxide per average particle size fraction (a) SiO_2, Al_2O_3 and CaO, and (b) Cr_2O_3, MgO, MnO and V_2O_3.

3.6 Tapping rate

In order to reduce the generation of fines (-106 µm fraction) during the handling of slag, high slag tapping rates were shown to be beneficial. Tapping rate, in turn, depends on factors which can be grouped into three categories (i) those external to the smelting process, e.g. taphole diameter and taphole opening and closing practices (ii) physical conditions within the furnace, e.g. bank formation and slag level, and (iii) physico-chemical and energy (temperature) properties of the slag at the time of tap. The following follows from an investigation into the chemical and energy properties of the slag which could impact on the slag at the time of a tap.

The characteristic FeO-TiO_2-Ti_2O_3 relationship of the titanium dioxide slags is well documented and investigated[26]. A comparison between the normalised components $\%TiO_2$, equivalent $\%Ti_2O_3$ and equivalent %FeO as produced during Campaign 9 and at the plant is given in Figure 53. Slags from both sources follow the same relationships between these three components. Hence any correlation between the tapping rate and one of these three major slag composition components should extend to the other two components as well. Since the slag is in the liquid phase during tapping the solid phase mineralogical components ilmenite, rutile, etc. were not considered.

With the components MnO, MgO being included with the equivalent %FeO, and Cr_2O_3, V_2O_5 and Al_2O_3 being included in the equivalent $\%Ti_2O_3$, the only other significant chemical components are SiO_2, CaO and the remainder of the Al_2O_3 which does not report to the equivalent $\%Ti_2O_3$. These components are grouped together into the glass phase. For the purposes of this investigation, the $\%SiO_2$ was selected as representative component of the silicate phases.

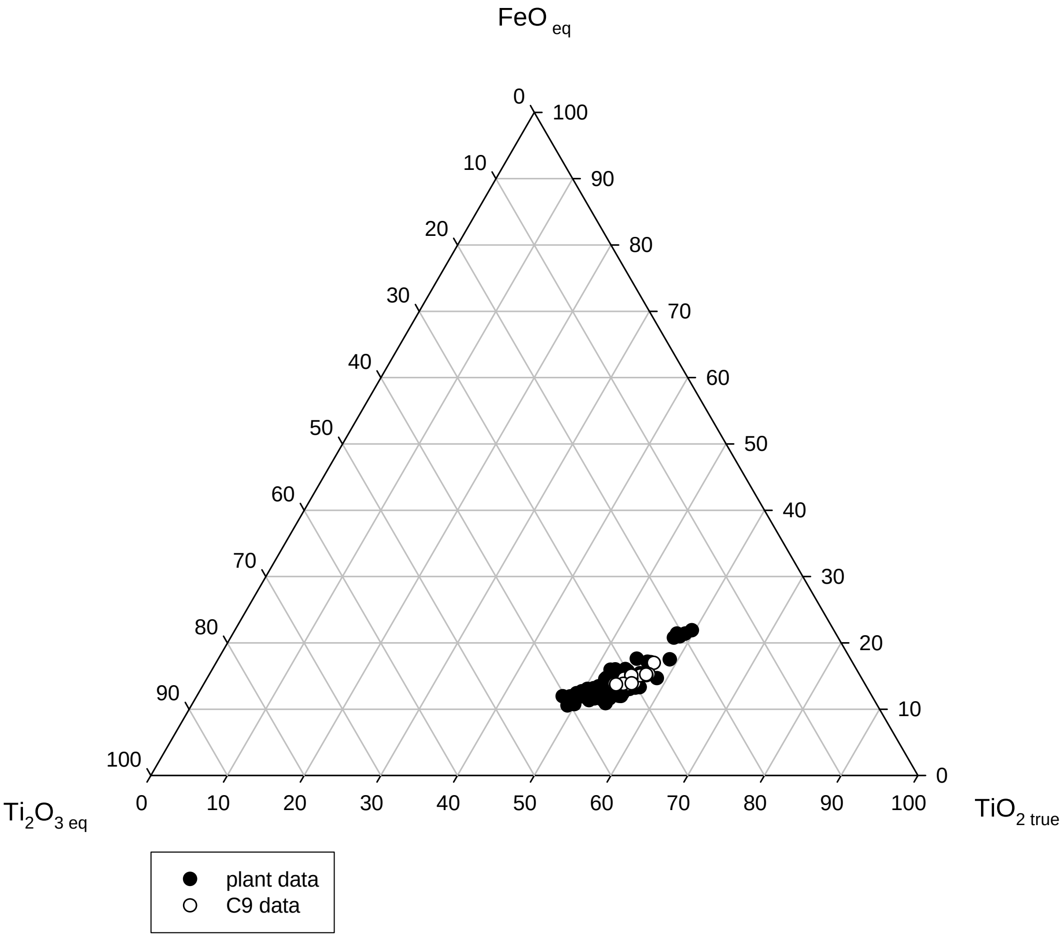

Figure 53 Relationship between equivalent %FeO, equivalent %Ti_2O_3 and %TiO_2 of slags produced at the pilot facility during campaign 9 and at the industrial scale plant.

3.6.1 Method

During a sampling trial the tapping rate of each pot from 43 taps made from the industrial scale furnaces was measured and recorded (one tap consisting of anything from 1 to 3 pots). For each pot a slag sample was taken at the lower end of the launder (Figure 54). As part of the hypothesis that oxidation plays a determining role in the final particle size distribution of the slag, the extent to which the sample is exposed to air is relevant. Samples taken at the end of the launder were therefore exposed to the oxidation conditions prevailing up to, and including flow over the launder. This includes exposure to oxygen lancing – which is used more extensively during slow taps in an attempt to encourage flows.

However, the oxidation level of these samples does not include further oxidation as the slag flows from the launder tip into the pot. Examples of the appearance of the tapping stream during fast and slow tapping are shown in Figure 55. During fast tapping the outer layers of the slag stream shield the core of the stream against oxidation; while the whole of the tapping stream of a slow tap – often individual droplets as in Figure 55(b) - is exposed to air. The probability of oxidation during a slow tap is therefore considerably higher than for a fast tap. However, the extent of oxidation in the falling slag stream was not quantified due to difficulties in obtaining safe access, preventing re-sampling from the pot.

The tap samples were analysed with XRF and wet chemistry – the latter to determine the Ti^{3+} content.

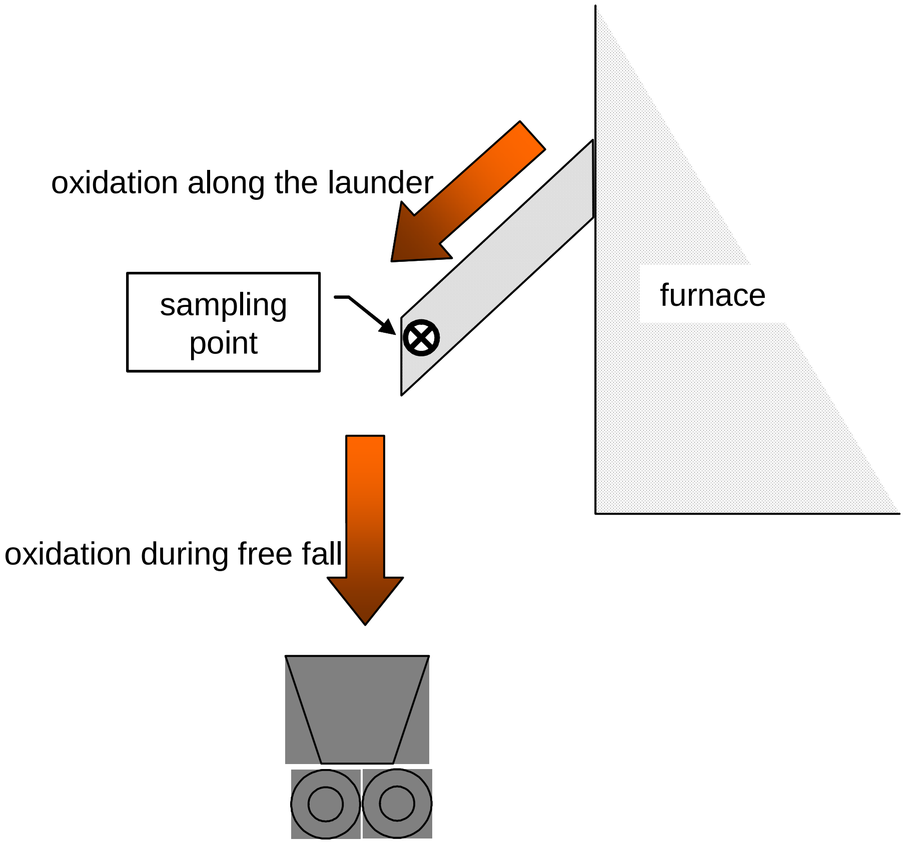

Figure 54 Sketch of the tapping system layout.

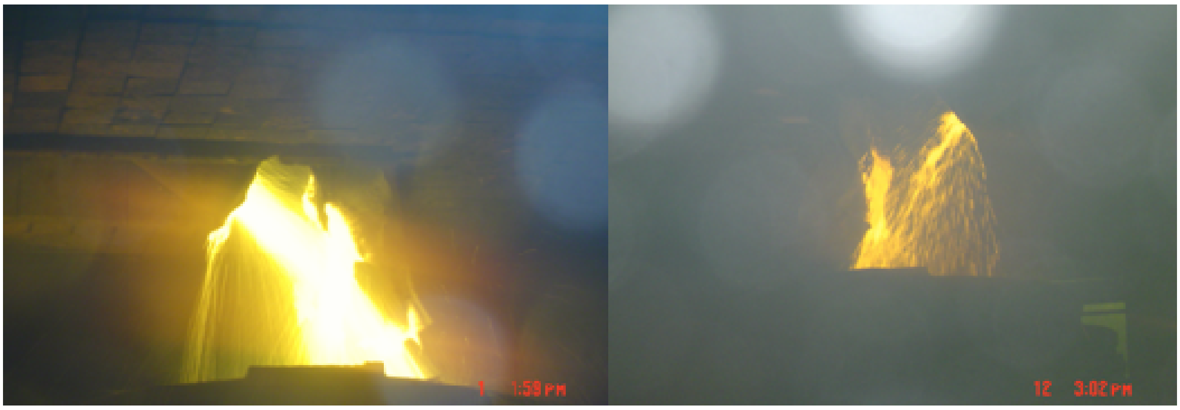

(a) (b)

Figure 55 Photographs of the tapping stream of (a) a fast and (b) a slow tap.

3.6.2 Results

The tapping rate as a function of %Ti_2O_3 is given in Figure 56. A weak tendency for the tapping rate to decrease with increasing %Ti_2O_3 is apparent. Although there does appear to be a stronger correlation between the $\%Ti_2O_3$ and superheat[§§] (Figure 58), this correlation does not extend to tapping rate vs. superheat (Figure 57).

From Figure 59 a slight decrease in the equivalent $\%Ti_2O_3$ for a given %FeO is apparent with slower tapping rates. Partial oxidation (of Ti^{3+} to Ti^{4+}) occurring up to the lower end of the launder is therefore implied. The occurrence of further oxidation is evident further downstream in the process: the trendline in Figure 59 for the cooled blocks shifts to even lower equivalent $\%Ti_2O_3$ levels for a given equivalent %FeO level.

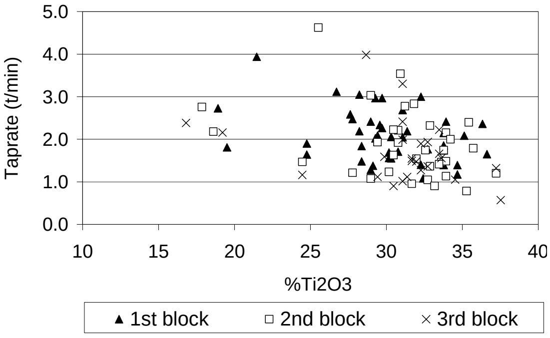

Figure 56 Tapping rate vs. $\%Ti_2O_3$.

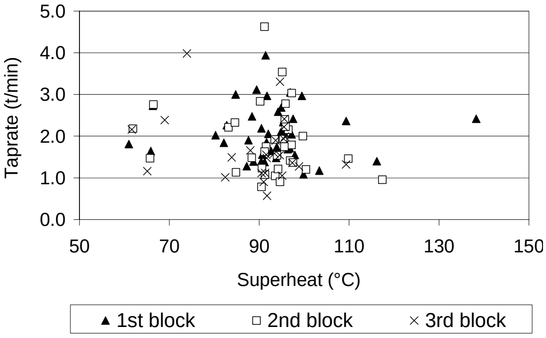

Figure 57 Tapping rate vs. superheat.

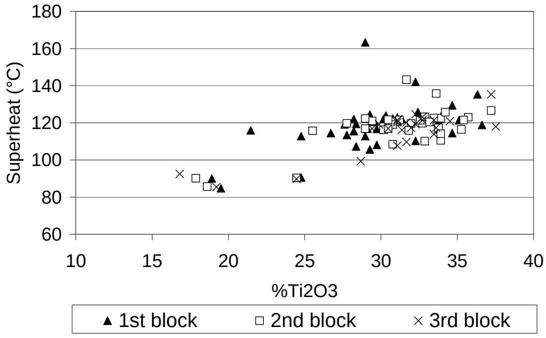

Figure 58 Superheat vs. $\%Ti_2O_3$.

[§§] Superheat is defined as the temperature difference between the tap temperature and the calculated liquidus temperature for the given slag analysis. Details on the calculation of the liquidus temperatures are given in Part 3.

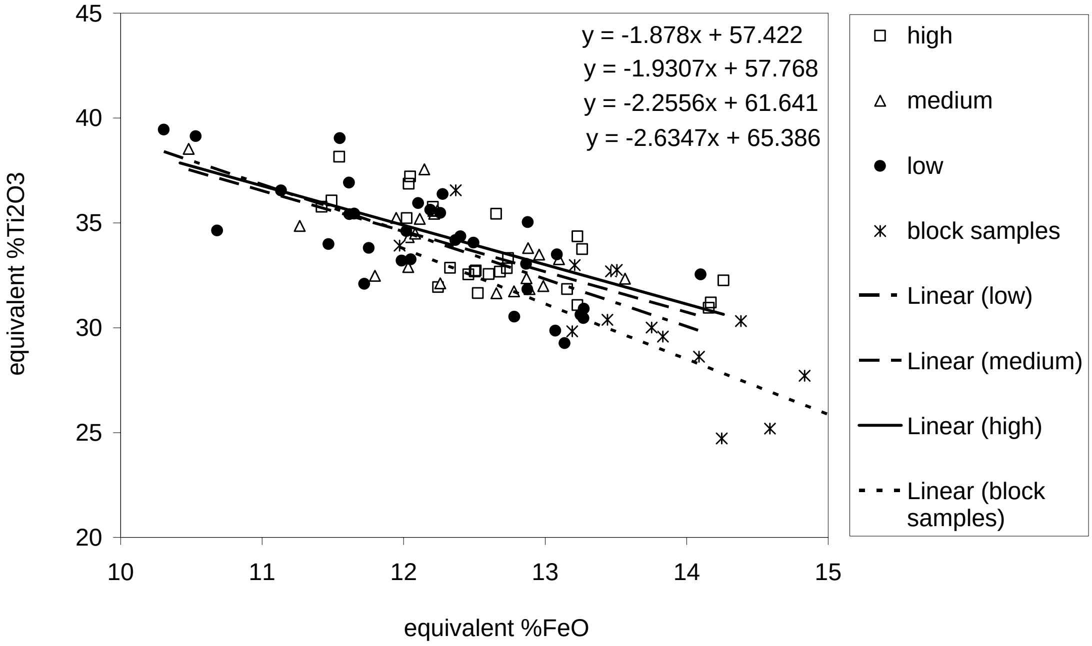

Figure 59 Equivalent %FeO vs. equivalent %Ti_2O_3 grouped for high, medium and low tapping rates. Also shown is the ratio for samples taken from the blocks following cooling in the block yard. The order of the correlations in the upper right corner corresponds with the order of the legend.

The shift in composition during oxidation is explained by the work of Pistorius et al.[4,22] with rutile being a reaction product of oxidation at temperatures in the solidification range of titania slags (Figure 3 and repeated here for ease of reference as Figure 60) and solid state temperatures (Figure 61). (Note that compositions are plotted as mole fractions in these figures). A typical slag composition lies at approximately 0.58 mole fraction $TiO_2/(TiO_2+FeO+Ti_2O_3)$ on the x-axis in Figure 60. On oxidation of the slag in the solidification temperature range, the slag composition moves toward the right of Figure 60 (with Ti_2O_3 decreasing and TiO_2 increasing proportionally) resulting in the formation of rutile.

Similarly, during oxidation in the solid state the initial slag composition moves along the oxidation path to the right of Figure 61 (with fully oxidised TiO_2 and Fe_2O_3 as the final reaction products). In the case of titania slag blocks the oxidation reaction does not progress into the FeO-$FeO_{1.5}$-TiO_2 system, but it does lead to an increased proportion of rutile, as expected from the shift in intersection point between the oxidation path and the M_3O_5-rutile tie line.

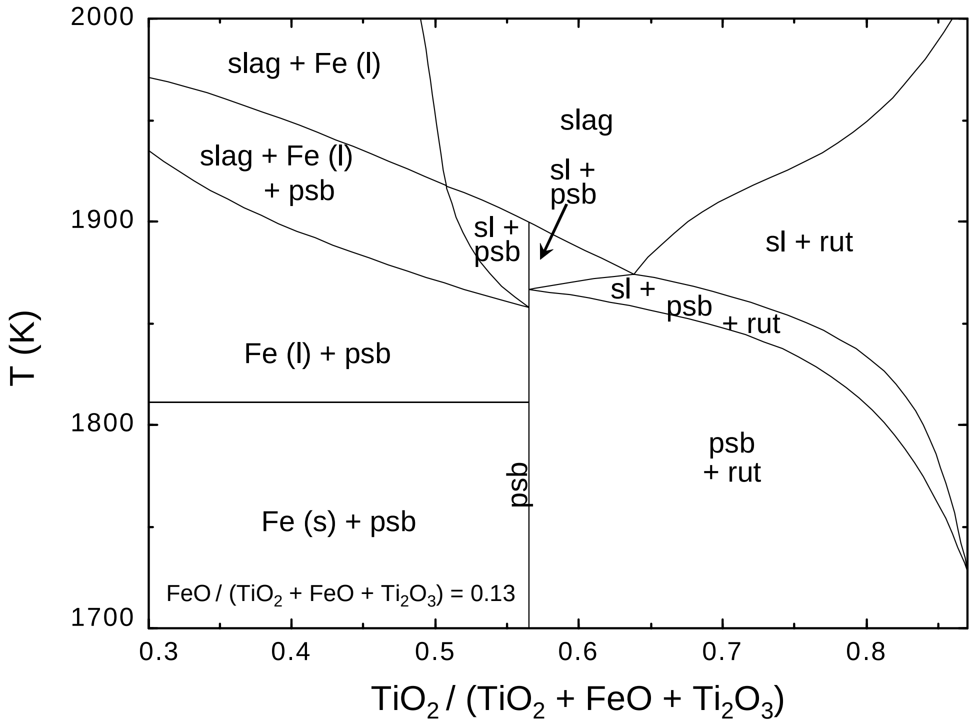

Figure 60 Calculated section through the TiO_2-Ti_2O_3-FeO phase diagram, at a constant FeO mole fraction of 0.13 (assuming that Magnéli phases are absent). Phases are identified as follows: "sl" is the molten oxide (slag), "psb" is the M_3O_5 phase, "rut" is the rutile-based solid solution (TiO_2 with some Ti_2O_3 in solution), and "Fe" is metallic iron[4].

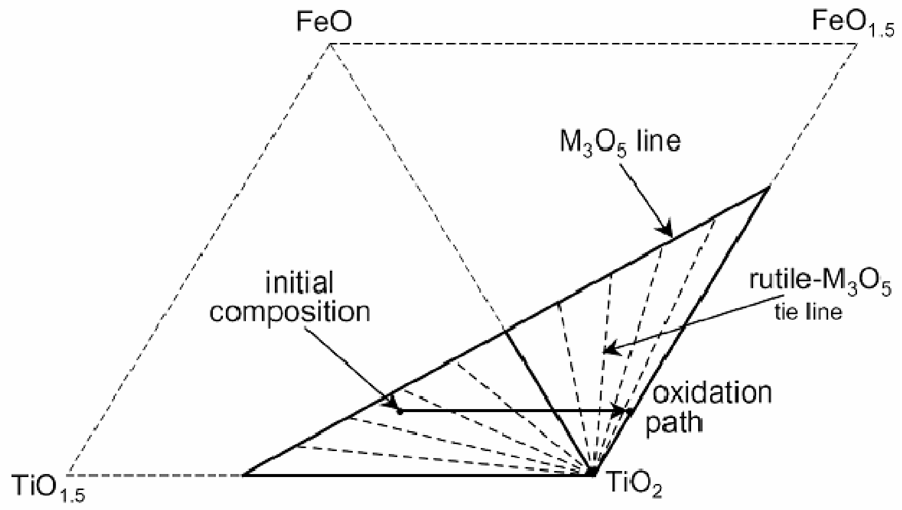

Figure 61 Change in phase relationships in high-titanium slag during solid-state oxidation above 550°C[4].

From Figure 62 the tapping rate does not appear to be a strong function of the $\%SiO_2$. It is interesting to note the strong correlation between %FeO and $\%SiO_2$ (Figure 63). The correlation coefficient between $\%SiO_2$ and %FeO is very strong at -0.906. (The correlation coefficients between the $\%SiO_2$ and $\%TiO_2$ or $\%Ti_2O_3$ are 0.866 and 0.780 respectively.) At FeO contents above 10% this correlation seems to be less pronounced. This correlation cannot be explained by a dilution effect: removing 1 mass% of FeO from the slag and increasing the equivalent %TiO_2 as per the correlation in Figure 53, while keeping the other oxide units constant, would increase the SiO_2 from 1.165% to 1.166% - an insignificant effect. The linear correlation in Figure 63 predicts an increase in excess of 0.05% SiO_2 for every 1% increase in FeO.

A possible explanation for the strong correlation between SiO_2 and FeO is the relationship between the reductant added to the process and the level of reduction in the slag: in the ilmenite smelting process the slag composition is mainly controlled with the amount of reductant added (in the form of anthracite) to the slag bath. Typically 30% to 45% of the total SiO_2 input into the process originates from the anthracite, of which close to 45% ends up in the titania slag (the remainder of the SiO_2 reports to the process dust and liquid metal). The strong correlation between the %SiO_2 and %FeO does not appear in the Campaign 9 data (Figure 64).

Hence, although the effect of SiO_2 on fines formation can be an indirect result of differences in the tapping rate (which in turn is presumed to depend on the major chemical components of the slag, notably the FeO level), it is not clear that this is the mechanistic link. The microstructural effects – of cracks associated with silicates (SiO_2 level) and rutile (present because of oxidation during tapping) – are much more evident.

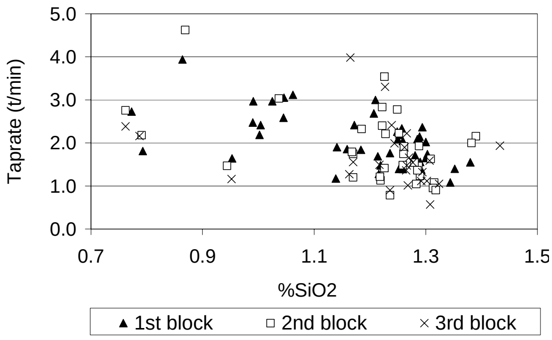

Figure 62 Tapping rate vs. %SiO_2.

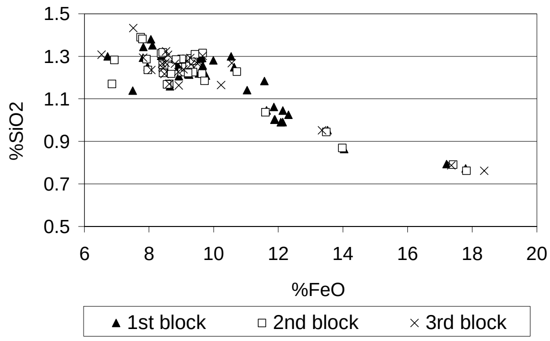

Figure 63 %FeO vs. %SiO_2.

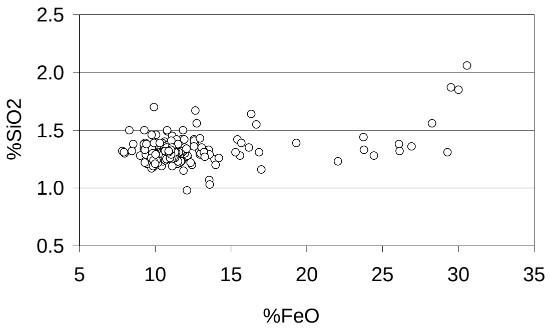

Figure 64 %FeO vs. %SiO_2 from campaign 9 data.

3.7 Surface temperatures

The average surface temperatures of the two blocks cooled under water for 3 days only are given in Figure 27. Although the two blocks were tapped 5 hours 9 minutes apart, they were tipped out of the pots 20 minutes apart. The surface temperatures of the two blocks ran remarkably close together – both reheated to approximately 90 ˚C some 105 - 106 hours after tipping, and again to 72 ˚C after approximately 125 hours after tipping. From 140 hours after tipping onwards, the surface temperatures remained below 50 ˚C and followed the variation in the ambient temperatures.

Since the spray water circuit was open to atmosphere, the temperature of the spray water is assumed to be equal to ambient temperature; and hence the surface temperatures of the blocks cooled under water for the full 10 days were also assumed to be close to ambient temperature.

The surfaces of all four blocks experienced little or no exposure to typical temperatures where decrepitation occurs[5,6] - limited decrepitation was therefore expected. However, as in the case of the pilot plant blocks discussed in Part 1, the blocks with an inferior cooling history resulted in higher fines generation during handling (Figure 34) and a larger variation in particle size distributions (Figure 44 and Figure 45). Should an oxidation mechanism be the cause of this – as suggested by the difference in %Ti_2O_3 between the tap samples and corresponding block samples (Figure 59) – it appears that oxidation occurs at temperatures as low as 100 ºC. This was tested by performing X-ray diffraction while the sample was exposed to air at 100 ºC, as reported in this section.

3.7.1 Method[***]

Finely ground samples of the four blocks were subsequently exposed to air at 100 ºC for prolonged periods and analysed for possible oxidation products. Initial experimental work on four samples from each block oxidised for periods of 2, 4, 7 and 15 days showed phase percentages within the range of sample heterogeneity. The heterogeneity of the samples was confirmed by a series of tests which served to evaluate the error in the machine (tested by re-analysing the same sample), error in sample preparation (tested by re-mounting the same sample) and error in sub samples (tested by analysing different sub-samples). The variation in sample composition was removed by exposing one sample from block L2R9 (fast tapped, 10 days water cooling) and L1R11 (slow tapped, 3 days water cooled) each, for in-situ XRD analysis at 100 ºC in an Anton Paar heating chamber using a platinum heating strip. Initially 8 measurements were done every 15 minutes, then 4 measurements every 30 minutes, and finally 8 measurements every 8 hours.

3.7.2 Results

The phase percentages over time are given in Figure 65. The M_3O_5 content of block L2R9 remains fairly constant over the duration of the oxidation period. A slight decrease in M_3O_5 is possible after approximately 40 hours which appears to be mirrored in the increase in the amount of amorphous phase. At 3.5 hours at 100 ºC the M_3O_5 in the sample from block L1R11 decreases significantly, with an accompanied increase in the amorphous phase. A slight decrease in rutile and anatase also appears at this time. No similar behaviour is apparent in the sample from block L2R9. After cooling for 10 days in water the mineralogy of block L2R9 appeared to have stabilised, while that of block L1R11 still shows the potential to oxidise further, transforming M_3O_5 to a weakly crystalline phase – possibly a forerunner of the M_6O_{11} phase. It is inconclusive on whether the faster-tapped and 10 day water-cooled block L2R9

[***] This work was conducted by Professor J. de Villiers of the Department of Materials Science and Metallurgical Engineering of the University of Pretoria.

has a more stable phase composition due to its tapping rate or to the more intense water cooling – or both.

It is however conclusive that oxidation can occur in a block at temperatures as low as 100 ºC. It furthermore appears that the tendency for this to occur is a function of the block history.

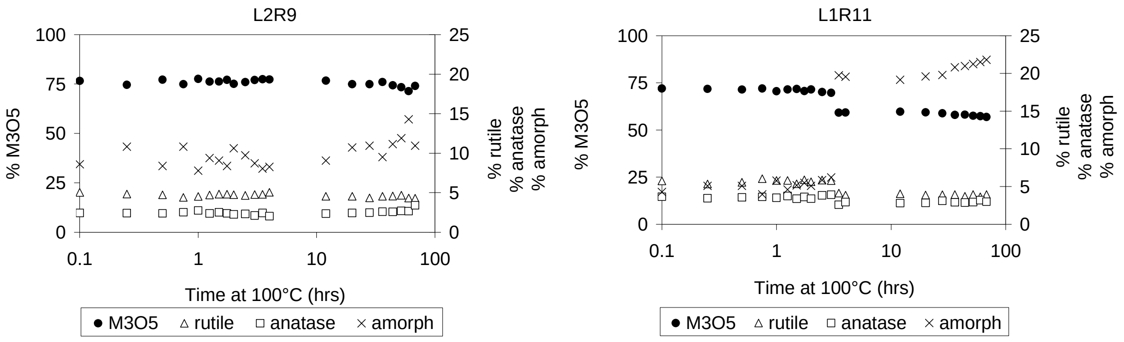

(a) (b)

Figure 65 Mineralogy of blocks (a) L2R9 and (b) L1R11 when exposed to air at 100 ºC.

3.8 Conclusions

The findings of Part 2 confirm the importance of the glass phase, tapping rate and cooling history on the final particle size distribution of a slag block.

A higher tapping rate reduces the extent of fines generated during materials handling. The mechanism behind this phenomenon appears to be driven by oxidation of the slag during the various processing steps. Extensive solid-state oxidation of the M_3O_5 phase to M_6O_{11} is known to cause formation of very fine particles. However, from the preceding results it is clear that more subtle forms, or less advanced stages of oxidation, influence the particle size distribution of a slag block. Such solid-state oxidation can occur at high temperatures, e.g. during tapping, during intermediate temperatures, e.g. initial cooling of the block, or at relatively low temperatures – of the order of 100 ˚C or lower. Although a link between oxidation and particle size distribution is obvious, the mechanism is still unclear.

Such oxidation can be suppressed with intensive water cooling. Apart from decreasing the block surface temperature to levels where the reaction kinetics is retarded, intensive water cooling seems to enhance phase stability. This is in contrast with insufficiently cooled slag which showed further oxidation at 100 ˚C.

Practical implementation of the above knowledge requires quantification of “intensive” and “insufficient”. This is addressed in Part 3.

The variation in particle size distribution of an intensely water cooled block is furthermore much less. Insufficiently water cooled blocks hence require broader operating ranges and equipment settings – preventing the attainment of optimum processing conditions which are required to maximise the ratio of the higher valued chloride to fine grade slag.

Of all chemistry parameters, the effect of the silicate phases is predominant in determining the particle size distribution. From the preceding results it is clear that the silicate phases are trapped during solidification between the karrooite (M_3O_5) granules. On subsequent breakage, intergranular breakage liberates some of these silicate phases while some remain attached to the surface of the coarser grains. The narrow range of silicate content within the samples used in this study does not provide an answer to the question as to how higher silicate levels would affect the grain size of the crushed and milled karrooite.